TRIBHUVAN UNIVERSITY
INSTITUTE OF ENGINEERING
PULCHOWK CAMPUS

EXPERIMENTAL STUDY OF LEADING-EDGE SINUSOIDAL TUBERCLES ON NACA 63215 WING AT LOW REYNOLDS NUMBER

By:
Bishowdip Khadka (077BAS009)
Lujaa Maharjan (077BAS020)
Pradeep Saud (077BAS028)
Sewak Timalsina (077BAS040)

FINAL YEAR PROJECT REPORT
SUBMITTED TO THE DEPARTMENT OF MECHANICAL AND AEROSPACE ENGINEERING IN PARTIAL FULFILLMENT OF THE REQUIREMENT FOR THE DEGREE OF BACHELOR IN AEROSPACE ENGINEERING

DEPARTMENT OF MECHANICAL AND AEROSPACE ENGINEERING
LALITPUR, NEPAL

March 5, 2025

ABSTRACT

Owing to the reputation of humpback whale flippers in delaying stall and improving the post stall performance, four different wings at Reynolds Number of 85,000 with varying leading-edge profile on NACA 63215 was experimented on open section Wind Tunnel. The wing with varying amplitudes and wavelengths was configured to observe the effect of sinusoidal waves on the aerodynamic behavior of the wing. The tubercles' leading edge (TLE) alters the boundary layer behavior, delays the stall, and enhances the post-stall behavior of the wing by the counter-rotating vortex in the trough of the wave that reattaches the separated flow during and after the post-stall region, resulting in a delayed stall. The sinusoidal alternating wave pattern on the wing compartmentalizes the flow, and the non-stalled crest portion of the wing is unaffected by the separated flow at the trough. The larger amplitude creates softer stall characteristics by maintaining attached flow at peaks despite the separated flow at the trough. Instead of the entire wing suddenly stalling, the alternating pattern of waves results in a gradual loss of lift. By comparing the results of baseline wings and tubercles wings, this study aims to provide information on the effectiveness of modifications in the wing as a passive flow control device to improve aerodynamic efficiency at low-speed flight. Since the γ-*Re* θ SST turbulence model provides a transitional flow from laminar to turbulent ranging from an Angle of Attack 8° to 24° with increments of 4°, it was utilized in ANSYS to perform the flow behavior analysis. The leading-edge tubercles result in a drag decrement by 12% at the stall regime and lift enhancement by 17% with stall delayed by 6°. The findings of the results could contribute to the development and understanding of fluid dynamics in bio-inspired engineering.

Keywords: Counter-Rotating Vortex, Passive Flow Control, Post-Stall, Softer Stall, Tubercles Leading-Edge (TLE)

LETTER OF APPROVAL

TRIBHUVAN UNIVERSITY
INSTITUTE OF ENGINEERING
PULCHOWK CAMPUS
DEPARTMENT OF MECHANICAL AND AEROSPACE ENGINEERING

The undersigned certify that they have read and recommended to the Institute of Engineering for acceptance, a project report entitled **"EXPERIMENTAL STUDY OF LEADING-EDGE SINUSOIDAL TUBERCLES ON NACA 63215 WING AT LOW REYNOLDS NUMBER"** submitted by Bishowdip Khadka (077BAS009), Lujaa Maharjan (077BAS020), Pradeep Saud (077BAS028), and Sewak Timalsina (077BAS040) in partial fulfillment of the requirements for the degree of Bachelor of Aerospace Engineering.

.....
Supervisor, Er.. Chiranjivi Dahal
Assistant Professor
Department of Mechanical and Aerospace Engineering
Institute of Engineering, Pulchowk Campus

.....
External Examiner, Er. Bibek Dhungana
Assistant Professor
Institute of Engineering, Thapathali Campus

.....
Head of Department, Dr. Sudip Bhattrai
Assistant Professor
Department of Mechanical and Aerospace Engineering
Institute of Engineering, Pulchowk Campus

Date: 10 Mar 2025

ACKNOWLEDGMENT

This project has been prepared as a partial requirement for the completion of a bachelor's degree in Aerospace Engineering.

First and foremost, we are most thankful to our project supervisor, Assistant Professor Chiranjivi Dahal. His constructive criticism and valuable suggestions have enabled us to mold our work. Were it not for his constant guidance and support, this experience would have been far more challenging.

We also express our sincere gratitude to Assistant Professor Dr. Sudip Bhattarai, Head of the Department of Mechanical and Aerospace Engineering, for his technical recommendations and remarks, which helped in refining our project significantly.

We greatly appreciate the guidelines of Assistant Professor Kamal Darlami, Deputy Head of the Department of Mechanical and Aerospace Engineering and Head of the Incubation, Innovation, and Entrepreneurship Centre (IIEC). His instruction in flow visualization and unconditional support have been of great benefit to our research.

Over and above that, our heartfelt gratitude goes to the Incubation, Innovation, and Entrepreneurship Centre (IIEC) for providing essential resources and a conducive environment that supports innovation and entrepreneurial growth.

Lastly, we would like to thank the Department of Mechanical and Aerospace Engineering and all our friends and families who have directly and indirectly helped us complete this project. Any kind of suggestion or constructive criticism will be appreciated and acknowledged.

Bishowdip Khadka (077BAS009)

Lujaa Maharjan (077BAS020)

Pradeep Saud (077BAS028)

Sewak Timalsina (077BAS040)

TABLE OF CONTENTS

LIST OF TABLES

LIST OF FIGURES

LIST OF ABBREVIATIONS

AOA	Angle of Attack
CFD	Computational Fluid Dynamics
e	Energy
FEA	Finite Element Analysis
g	Acceleration due to Gravity
GND	Ground
IDE	Integrated Development Environment
LE	Leading Edge
NACA	National Advisory Committee for Aeronautics
NASA	National Aeronautics and Space Administration
p	Pressure
PLA	Polylactic Acid
Re	Reynolds Number
SST	Shear Stress Transport
TKE	Turbulence Kinetic Energy
TLE	Tubercles Leading-edge
UAV	Unmanned Aerial Vehicle

NOMENCLATURE

Symbol	Description
α	Angle of attack (degrees)
c	Chord length
C_D	Drag coefficient
C_L	Lift coefficient
ε	Epsilon (Turbulence dissipation rate)
γ	Gamma (Intermittency)
I	Current
k	Turbulent Kinetic Energy
L	Characteristic length
λ	Lambda (Wavelength)
μ	Mu (Dynamic viscosity)
∇	Nabla (Vector differential operator)
ω	Omega (Specific dissipation rate)
R	Resistance
ρ	Rho (Air density (kg/m^3))
S	Wing area (m^2)
t	Time
τ	Tau (Shear Stress)
θ	Theta
V	Velocity

CHAPTER 1:
INTRODUCTION

1.1 Background

Aerodynamics has evolved from basic trial-and-error methods to sophisticated, multi-disciplinary research. Tracing back to the work of the Wright brothers in the early 20^{th} century, they struggled to understand the forces of lift and drag because of inadequate and sometimes inaccurate traditional theories and data, so they conducted experiments using a wind tunnel they built in 1901 (4). This tunnel allowed them to test different airfoil shapes and better understand the relationship between lift and drag, which became the breakthrough of their successful flight designs.

As research in aerodynamics progressed, wind tunnels became inevitable in studying and improving flight performance. One of the first large-scale wind tunnels was developed by NACA in 1922, using which researchers achieved higher Reynolds numbers and more accurate data at lower velocities. Over the years, institutions like NASA Ames Research Center housed some of the world's largest and most versatile tunnels capable of testing both aircraft and spacecraft models (5).

Aerodynamic forces, lift, thrust, weight, and drag determine the dynamic balance of an aircraft. Lift acts perpendicular to airflow and is generated due to a pressure difference between the upper and lower surfaces of the wing. As air flows over the upper curved surface of the wing, it accelerates and creates a region of lower pressure compared to the flat lower surface, which results in a net upward force (6).

$$L = \frac{1}{2}\rho V^2 S C_L \tag{1.1}$$

Where, L represents Lift force
C_L represents Lift coefficient
ρ represents Air density
V represents Airspeed
and S is Wing area

Likewise, drag opposes the motion of an object and is caused by friction between the air and the surface of the object (skin friction drag) and the disruption of airflow around the object (pressure drag). Pressure drag is further subdivided into form drag, resulting from the shape of the object, and induced drag, caused by the generation of lift. Drag is typically measured parallel to airflow and is determined by airspeed, shape, and surface roughness (6).

$$D = \frac{1}{2}\rho V^2 S C_D \tag{1.2}$$

Where, C_D is Drag Coefficient

The pressure distribution across the wing varies per the shape, angle of attack, and airspeed. As per Bernoulli Distribution:

$$P + \frac{1}{2}\rho V^2 = Constant \tag{1.3}$$

1.1.1 Wing Tubercles

At high angles of attack, conventional wings experience flow separation and stall, for which flow control mechanisms are required. Active flow control systems such as flaps and slats manage airflow however, they demand continuous power input, which makes them less efficient for certain applications. Contrarily, passive flow control techniques modify airflow behavior naturally without requiring external energy; thus, they are more efficient alternatives.

On this matter, wing leading edge tubercles, inspired by the morphology of humpback whale flippers, can be taken as passive flow control devices (7),(8). They are known to prolong flow attachment, increase post-stall lift, and provide smoother stall characteristics, all of which make tubercles a promising design feature for improving aerodynamic performance, especially for high maneuverability and delayed stall (9).

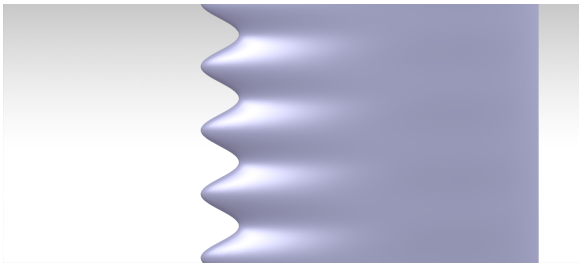

Figure 1.1: Leading Edge Wing Tubercles

The associated aerodynamic phenomena arise from the formation of stream-wise counter-rotating vortex pairs behind each tubercle, and such vortices result in the following effects:

- **Momentum Exchange and Boundary Layer Energization:** The vortices transfer momentum from the free stream into the boundary layer, thus delaying flow separation and increasing stall angle (10).
- **Flow Compartmentalization:** The flow is divided into distinct channels between adjacent tubercles, which ultimately minimizes the span-wise flow component, limits the degree of flow separation, and reduces aerodynamic losses (11).
- **Wake Modification:** Tubercles confine flow separation to the areas behind troughs. It minimizes chaotic turbulence and weakens large-scale wake effects (10).

1.1.2 Mechanism of Action

Tubercles create a wavy leading edge that redirects free flow into the troughs. This causes stream-wise counter-rotating vortex pairs (12) to be generated that suppress large-scale separation and promote gradual stall behavior by increasing mixing and re-energizing the boundary layer.

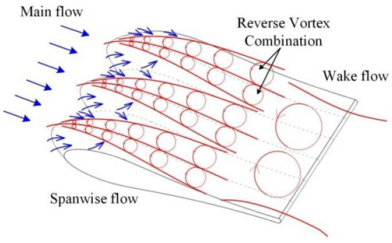

(a) Span-wise flow over wavy surface (13)

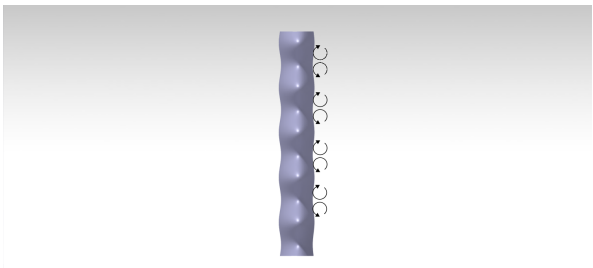

(b) Stream-wise counter-rotating vortex pairs

In the presence of opposite-signed vortex, rotational energies cancel out, which is known as vortex annihilation. However, positive vortex, being stronger ones, persist and move downstream into the wing's wake. They interact with trailing-edge and tip vortex and influence overall aerodynamic characteristics.

- Tubercle leading edges (TLE) have been observed to increase lift by 14-19% at $25^\circ - 30^\circ$ AOA depending on the specific amplitude and wavelength (14).

- General span-wise flow impacts vortex behavior. Negative tubercle vortex often annihilate, whereas positive vortex endure in the downstream wake. Consequently, the trailing edge vortex sheet is disrupted, and energy from the tip vortex is withdrawn, leading to a weakened tip vortex with reduced intensity.

- Near the wingtip, co-rotational interactions occur between tubercle-generated vortex (likely positive) and the dominant tip vortex. The stronger one absorbs smaller tubercle vortex by merging their energy into a reorganized wake structure. Finally, the tip vortex weakens, and its destruction diminishes lift-induced drag.

- For straight leading edge wings, flow separation is more severe across the entire trailing edge and extends forward to the leading edge. Meanwhile, tubercle crests compartmentalize separation by forming strong counter-rotating vortex structures in each channel. Such structures are born from tubercle vorticity and interact with tip vortices, triggering long-wavelength instabilities along the wake path.

- Weakened tip vortices show increased circulation and suggest for partial diffusion. This phenomenon could help lower wingtip drag and improve aerodynamic efficiency at higher AOA.

1.1.3 Turbulence Kinetic Energy (TKE)

TKE experiences an energy cascade to smaller scales through eddy interactions. In wind tunnel experiments, this process helps understand turbulent flows interacting with the wing surface. At very small scales, viscosity dominates, and the TKE dissipates into heat, affecting aerodynamic performance and the boundary layer characteristics.

1. Boundary Layer Effect

   High energy near the wing surface leads to faster energy dissipation, which can result in an earlier onset of flow separation (8). This is particularly important for high-speed airflow over the wing in wind tunnel tests, as it may influence the aerodynamic stall characteristics.

   Contrarily, near-surface low energy helps to maintain turbulence and consequently postpone flow separation. This can refine the overall lift and performance, mainly where maintaining a stable flow is necessary to prevent stalling.

2. Vortex Strength

   Vortex strength directly alters the longevity and intensity of the vortices. Where Low dissipation of TKE results in stronger vortices, which help delay the stall by elevating flow reattachment, high dissipation leads to weaker ones, thereby limiting flow ability to re-energize. Such weakening of vortex strength can result in earlier flow separation and increased likelihood of stall; this is unfavorable.

1.1.4 The Need for CFD

CFD analysis delivers the numerical approximation to the equations that govern the fluid flow. The physical behavior of fluid flow is dictated by three fundamental principles: mass conservation, momentum conservation, and energy conservation. These principles are expressed as mathematical partial differential equations, which are discretized to create a numerical representation. The domain is divided into small grids or elements, and finally, the boundary conditions for the required problem are given to solve these equations (15).

The fundamental laws of fluid mechanics are used for the governing equations of the fluid. Here, the equation for the conservation of mass is given by:

$$\frac{\partial \rho}{\partial t} + \nabla \cdot (\rho \cdot \vec{V}) = 0 \tag{1.4}$$

Similarly, the equation of the conservation of momentum is given by:

$$\rho \frac{\partial \vec{v}}{\partial t} + \rho(\vec{v} \cdot \nabla)\vec{v} = -\nabla p + \rho \vec{g} + \nabla \cdot \tau_{ij} \tag{1.5}$$

Lastly, the equation of the conservation of energy is given by:

$$\nabla \cdot [\rho(e + \frac{\vec{V}^2}{2}) \cdot \vec{V}] = -\nabla \cdot (p\vec{V}) \tag{1.6}$$

These partial differential equations are approximated numerically by converting the Governing PDE to a linear algebraic form (15).

1.1.5 Wind Tunnel

Now that the theoretical concepts have been covered, experimental tests are a mandate to validate them. In this instance, wind tunnels, the controlled environments, simulate airflow's effects around objects. They consist of a closed passage with a fan or other mechanism to generate airflow, and models are placed in them with airspeed, pressure, and other parameters adjusted to replicate actual conditions. Wind tunnels are of two types: open circuit and closed circuit. In an open circuit, the air is taken from the atmosphere and expelled after passing through the test section. They are susceptible to external disturbances and require protective measures at the inlet (16), and their continuous operation consumes higher energy and creates noise levels, which can result in legislative restrictions. In the latter, the airflow is recirculated in a closed loop. They control flow parameters precisely, flow quality is unaffected by external factors, and require comparatively less energy to operate as airflow recirculates within the tunnel.

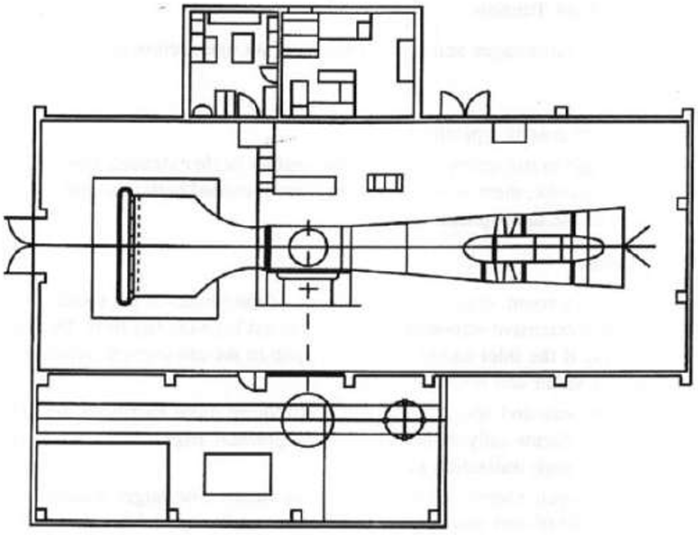

Figure 1.3: Open circuit Wind Tunnel (1)

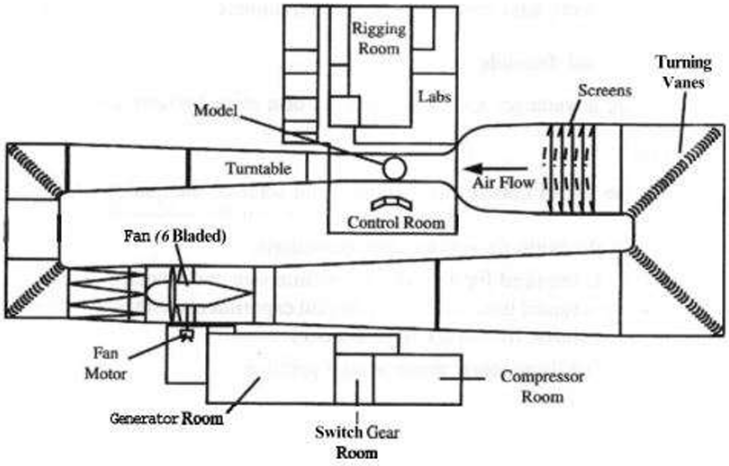

Figure 1.4: Closed circuit Wind Tunnel (1)

Wind tunnels come in various categories:

- Low-Speed Wind Tunnels
- Subsonic Wind Tunnels
- Transonic Wind Tunnels
- Supersonic Wind Tunnels
- Hypersonic Wind Tunnels.

Each type is designed for different testing conditions and flow velocities. For this study, experiments were conducted on the **Low-speed Open-Circuit Wind tunnel** available at the IOE Pulchowk Incubation Department (2). Given its outlet dimension of 120 cm x 52 cm and maximum flow velocity of 10 m/s, the specification is suitable for our test conditions.

Figure 1.5: Front View of Wind Tunnel (2)

Figure 1.6: Rear View of Wind Tunnel (2)

1.1.6 Load measurement systems

To measure the forces acting on the models in the wind tunnel, we use load measurement systems outfitted with strain gauges, load cells, and pressure sensors. These systems measure the lift, drag, and moments generated by the model, which are essential for validating theoretical aerodynamic models and refining aircraft design. Various types of force balances used for these measurements include:

- Pyramidal Balance
- Sting Balance Using Strain Gauges
- Direct Measurement Using Load Cells
- Simple Wire Hanger
- Six-Component Force Balance
- External and Internal Force Balance
- Force-Moment Balance

1.1.7 Wind tunnel balance

Global forces can be measured using different wind tunnel balances, local balances, or pressure distribution measurements. The parameters like range, accuracy, and response time of the measurement define these systems (16) and necessitate calibration along with measurement correction. Another method for the aerodynamic load measurement is the pressure measurement, which, while effective, is a complex and expensive process. The most important wind tunnel balances are:

- **External Balance**

  External balances always introduce some interference in the wind flow and are placed outside of the model, inside or outside of the wind tunnel test section. Several degrees of complexity exist, varying between 1 and 6, based on the number of components. An aerodynamic model is mounted to the calibrated balance system, which supports the model and transfers the forces and moments acting on it to the measurement system through mechanical linkages. Responses from

precision load sensors are recorded, and this raw data is then processed and converted into force and moment values to analyze the aerodynamic performance of the model.

- **Internal Balance**

  They are placed inside the model and hence do not have any interference with the wind flow. However, they still require support to remain stable in the test chamber. Normally, these balances are calibrated by the manufacturers and consist of 1 to 6 components.

In this experiment, the setup will include an external balance to measure aerodynamic forces, i.e., lift and drag, and CFD will validate the results obtained from the experimental analysis.

1.1.8 Load Cell

A load cell is a core component for measuring forces and moments acting on a model. It functions as a transducer converting mechanical energy into an electrical signal, which is measured through strain gauges attached to a metal body, 'spring element'. It operates on the principle of resistance change due to deformation; when a load is applied, the body undergoes slight deformations as measured by the strain gauges. The load cell follows the Wheatstone Bridge principle, which uses a configuration of four balanced resistors with a known excitation voltage.

If all resistors are balanced, meaning $\frac{R_1}{R_2} = \frac{R_4}{R_3}$ (17) then output voltage V_0 is zero. If there is a change in either of the resistor values, then V_0 will have a resulting change that can be measured and interpreted using Ohm's law (3). Ohm's law states that the current (I, measured in amperes) running through a conductor between two points is directly proportional to the voltage (V) across them. Resistance (R, measured in Ohms) is introduced as constant in this relationship, independent of current.
Mathemactically, $I = \frac{V}{R}$.

When applied to the 4 legs of the Wheatstone bridge circuit, the resulting equation

is (17):

$$V_{OUTPUT} = [\frac{R_3}{R_3 + R4} - \frac{R_2}{R_1 + R_2}] \times V_{EXCITATION} \tag{1.7}$$

In the load cell, these resistors are replaced by strain gauges in alternating tension and compression measurements. When a load is applied, the resistance in each strain gauge changes, and V_0 is measured.

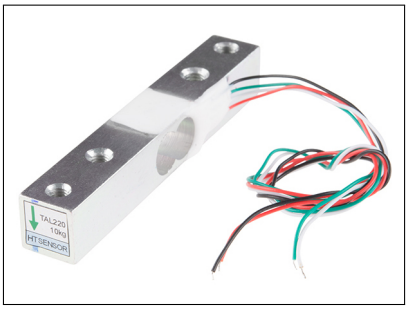

Figure 1.7: Strain gauge Load Cell (3)

The magnitude of the strain field produced by the force is determined by the geometry and elastic modulus of the element (18). Each element is designed to measure the force along the main axis and is not affected by other forces (such as side loads).

1.2 Problem Statement

Stall and boundary layer separation are problems with aerodynamic performance that result in less lift, more drag, and a loss of control. The bio-inspired wing Tubercles Leading Edge (TLE) features a passive flow control device that modifies the flow behavior by delaying the stall. Since the flow behavior is affected by the varying amplitude and wavelength of the tubercles' leading edge, wings with amplitudes of 3% and 6% of chord at various wavelengths of **0.1 c** and **0.2 c** have been created. In order to ascertain the effects of lift, drag, and stall behavior in the wing, this study is to examine the effect of the Tubercles leading-edge (TLE) on the aerodynamic characteristics of the NACA 63215 wing at low speed.

1.3 Objectives

1.3.1 Main Objective

The main objective of this project is to design and fabricate sinusoidal Tubercles Leading-Edge wings and to analyze their aerodynamic behavior in comparison with the baseline wing across pre-stall, stall, and post-stall regions.

1.3.2 Specific Objectives

1. Design and fabricate TLE (Tubercles leading-edge) wings and baseline wing using PLA + as printing material.
2. Model and fabricate the external balance along with its calibration in order to measure the aerodynamic forces of different wings in the wind tunnel.
3. Conduct an experimental test to analyze and compare the aerodynamic characteristics of baseline NACA 63215 wing and four wings of varying amplitude and wavelength with sinusoidal Tubercles Leading-Edge.
4. Perform CFD simulation using ANSYS to analyze and compare the aerodynamic forces and flow behavior of Tubercles Leading-Edge wings with baseline wing.
5. Visualize the flow behavior of baseline wing and tubercles wings in a wind tunnel using smoke and tuft.

1.4 System Requirements

1.4.1 Hardware Requirements

- Strain Gauge Load cell
- Arduino Uno Board
- HX 711 Amplifier
- 6200 2RS Deep Groove Ball Bearing
- PLA +

- Multi-Sized Nuts and Bolts
- Styrofoam
- Plywood
- Jumper Wires
- Protractor
- 8mm Threaded Rod
- 4mm Threaded Rod

1.4.2 Software Requirement

- ANSYS
- CATIA
- Arduino IDE
- Bambu studio

1.5 Scope of Research

- Understanding the effect of boundary layer separation, vortex generation, and flow control.
- Experimental studies to investigate the aerodynamic performance of wings with sinusoidal leading-edge tubercles, including lift and drag characteristics, stall behavior, and pressure distribution.
- Studying the optimal tubercles design for improving stall resistance and flow attachment.
- Investigating flexible, adaptive, and morphing surface that adjust tubercles geometry dynamically.
- Analyzing the influence in aeroacoustics to reduce noise.

1.6 Applications

- Improving stall resistance, maneuverability, and control for commercial and military aircraft.
- Using a smoke generator integrated into wind tunnels, flow visualization can be done to study the physics of flow around the tubercles
- Enhancing flight stability, efficiency, and endurance for low-speed drone operation.
- Enhancing the aerodynamic efficiency of wind turbine blades to improve energy output.
- Studying tubercles on ship propeller, hydrofoils and underwater control surface to minimize drag and cavitation.

CHAPTER 2:
LITERATURE REVIEW

Lift and drag are the primary aerodynamic forces acting on a body moving through a fluid. Lift is generated perpendicular to the flow direction due to pressure differences caused by surface curvature and angle of attack, whereas drag acts parallel to the flow and opposes motion (6). These forces depend on velocity, fluid density, surface area, and shape, which are encased in coefficients of lift and drag. And, these coefficients are essential for designing efficient aerodynamic structures.

An airfoil is a streamlined shape designed to generate lift by minimizing drag when moving through a fluid. The shape, its camber, and the angle of attack determine the pressure distribution over the surface and also govern the lift-to-drag ratio (4). So, airfoils are the basis for wings, blades, and other lifting surfaces, with their design being proportionate to overall aerodynamic performance.

When extending airfoil concepts to 3D wings, spanwise flow and induced drag phenomena come into action. Spanwise flow comes from pressure differences near the wingtips that generate vortices and lead to induced drag. To model these effects properly, augmented lifting-line methods have been developed by combining unsteady 2D aerodynamic data with the Kutta-Joukowski theorem to predict 3D wing forces. (19) With that, computational efficiency can be maintained, and effects like varied aspect ratio and reduced pitching motion frequencies can be captured. However, at very high reduced frequencies or in strong wake interference flows, the limitations of simplified methods become visible (20).

Flow control is a crucial area in aerospace engineering as it has the potency to optimize aerodynamic performance and efficiency. It broadly falls into two categories: active and passive flow control. Active flow control encases energy input to manipulate the flow field utilizing bio-inspired mechanisms and jet injection, whereas passive flow control relies on mechanical structures like riblets and grooves to alter boundary

layer characteristics (21). The main objective is to achieve benefits, say transition delay, lift increment, drag reduction, turbulence augmentation, and separation postponement. However, these parameters are often interdependent, meaning improvements in one aspect may lead to unintended negative effects on another (22).

The use of leading-edge tubercles in wing and blade designs, inspired by the natural structures found in humpback whale flippers, has been seen in several aerodynamic studies. These artificial tubercles, the waveform protrusion along wing's leading edge, improve performance characteristics dramatically, mainly in the pre- and near-stall regimes. In one of the studies, various tubercle geometries were tested, and it was found that the lift-to-drag ratio could be improved by up to 20 %, delay stall angles by approximately 4°, and get smoother pre- and post-stall behaviors. Such improvements resulted in the formation of counter-rotating vortices of tubercles, which helped reduce flow separation and maintain lift at higher angles of attack (14). Despite that, an increase in skin friction drag has been noted as a tradeoff.

To counteract it, tubercle leading-edge wing models are designed by studying their aerodynamic efficiency and comparing them with traditional ones (10). The simplicity of the geometry, which generally mirrors the form of delta wings, allows for easier manufacturing, thus making them an applicable solution for practical uses, say, UAVs. (14).

The tubercle performance mechanism is ascribed to counter-rotating vortex pairs that create alternating regions of upwash and downwash along the surface and, hence, the airflow distribution. Par to theoretical models, vortices with a common downwash move downward and away from each other, whereas those with a common upwash move closer together. This behavior contributes to a net aerodynamic benefit by reducing flow separation and elevating lift characteristics. Albeit numerous studies, the exact interaction between tubercle-induced vortices and overall wing aerodynamics is yet a subject of ongoing research (10).

Numerical and experimental studies suggest that tubercles can also improve maneu-

verability when it comes to systems requiring control surface efficiency. For instance, computations show that adding tubercles results in a high drag reduction alongside exalted lift and overall maneuverability at modest AOA (23). To mention specifically, this occurrence is advantageous for control surfaces where delay-stall capability and operational envelope extension results performance improvement. In structural studies, the tubercles in UAV wings have been calculated via finite element modeling, with findings signaling that such wings experienced lower deformation and stress than traditional designs. Also, the monocoque foam design had a 50. 72 % reduction in deformation and a 35.88 % decrease in stress; thus the tubercles could give lighter and more efficient wings (24).

Moreover, when the straight leading edge (LE) was modified with different combinations of amplitude and wavelength using SolidWorks and ANSYS-Fluent in NACA 2412, tubercles improved post-stall performance (5.33% increase in lift and a 2.72% reduction in drag at higher AOA. To be noted, the amplitude had a notable effect on performance than the wavelength, with larger amplitudes and smaller wavelengths being the most effective (25).

Based on this, further wind tunnel tests were conducted on wings with a sine wave LE. As a result, drag was reduced by 28%, and the lift-to-drag ratio had 48% increase post-stall. The study also brought in the concept of adjusting crest and trough widths so as to optimize performance. Furthermore, tubercles near the trailing edge, as seen in humpback whales' flippers, improved post-stall performance, although a fully sinusoidal trailing edge configuration yielded inferior results. The study's findings provide valuable design parameters for maximizing the aerodynamic benefits of tubercles (26).

Not only geometry but turbulence modeling approaches have also helped understand tubercle effectiveness in performance. When five different turbulence models: realizable k-ε, k-ω Shear Stress Transport (SST), ($\gamma - Re_\theta$) SST model, k-kl-ω model, and Stress-ω Reynolds Stress Model (RSM) were compared to simulate flow on a NACA0021 airfoil, simulations at a chord-based Reynolds number of 120,000 clarified that the Stress-ω RSM model estimated lift and drag coefficients closest to experimental results at

lower AOA, and at higher angles (16° & 20°), the k-ω SST model was more accurate. Hence, the latter model is better for capturing post-stall flow behavior and separated flow regions (27).

Furthermore, pressure contour analyses at lower AOA narrated that the Stress-ω RSM model predicted strong leading-edge suction effects, but the k-kl-ω model failed to predict accurate aerodynamic characteristics. This study insights us about the proper selection of turbulence models. And, on observing velocity streamlining for such models, the Stress-ω RSM model and k-kl-ω model failed to capture higher AOA flow behavior precisely (27).

Five-digit series airfoils, by default, have a maximum thickness of 50% of the chord (0.5 chords) from the leading edge. After several studies, the sinusoidal wavelength on the leading edge of NASA 65-021 and NASA 0021 airfoils' tubercle design were found to have a higher maximum lift coefficient and stall angle (28). In the numerical simulation of NASA 0012, leading-edge tubercles delayed stall at higher AOA and increased the maximum lift coefficient with Reynolds number (29). Adding up, the effect of protuberances on an S809 airfoil at Re 10^6 had a smoother stall transition than the baseline airfoil (30). A similar examination on the leading edge of NASA LS (1)-0413 had observable improvements in stall characteristics (31). Likewise, NACA 63215 features a maximum camber of 2% located 35% chords from the leading edge, and a maximum thickness of 15% of the chord. For numerical analysis, Gambit is used to create and generate 2D and 3D mesh files, which are then imported into Fluent for CFD simulations. In FLUENT 6.3.26, airfoil geometry undergoes analysis at different AOA like 4°, 8°, and 12° (32). The consensus shows that most of the studies are done in Reynolds numbers of 10^5 and above, leaving space for further exploration at lower Reynolds numbers.

The aerodynamic behavior of a wing depends on the flow regime given by the Reynolds number (Re), a dimensionless parameter that quantifies the ratio of inertial forces to viscous forces in the flow. Simply put (33),

$$Re = \frac{\rho u L}{\mu} \tag{2.1}$$

where ρ is fluid density, u is velocity, L is characteristic length, and μ is dynamic viscosity. Higher Reynolds numbers indicate dominant inertial forces leading to turbulent flow, and lower values correspond to laminar flow conditions.

In CFD, boundary layer behavior is resolved for accurate predictions of aerodynamic performance, for which the Y-plus (Y^+) value, another dimensionless quantity, is a must. It determines the placement of the first computational grid point near the surface and makes the capture of wall-bounded flow characteristics accurate (34).

$$y^+ = \frac{u_{\tau_{\text{air}}} y}{v_{\text{air}}} \tag{2.2}$$

where u_{air} is known as the friction velocity and is given by (35) $u_{\text{air}} = \left(\frac{\tau}{\rho}\right)^{\frac{1}{2}}$ (2.3)

For simulations requiring the resolution of the viscous sublayer, Y^+ values close to 1 are ideal, whereas wall-function approaches use higher Y^+ values (30 - 300) to reduce computational cost. The very concept is important for reliable CFD of boundary layer behavior, transition points, and induced drag effects because proper mesh design supported by Reynolds number and Y^+ considerations guarantees the reliability of results (34). Moreover, in low Reynolds number flow, resolving Y^+ value within the viscous sublayer is mandatory, and using a large first cell height is not recommended to cover the low law region, as doing so may incorrectly place grid points in that region (35).

Wind tunnel test is commonly performed to study various aerodynamic behaviors and boundary layer characteristics of scaled models (33). The models are placed in line to the inflow and mounted on a force balance system connected to a load cell for measuring loads exerted on them. In fluid dynamics, walls of wind tunnel, are sure to alter the flow behavior due to the "no-slip condition" since the velocity of fluid adjacent to the wall becomes zero. This disturbs the flow field around the test object, particularly for cases with high angles of attack or near-stall condition flows. To clarify further, the walls confine the airflow by limiting the lateral expansion (36), and consequently, the stream velocity around the model increases, and we can see the blockage effect. This

modifies the aerodynamic forces by resulting in increased lift and drag forces (30).

For an airfoil, such a phenomenon is important, as lift generation corresponds to flow circulation around the wing, which can be visualized as a system of bound vortex along its span. Interference from the confined stream in the tunnel alters the span lift distribution by inducing uncertainties in experimental measurements (36).

The aerodynamic effects of the wind tunnel walls become more defined when the distance between the airfoil and the walls is less than three times the chord length. They further intensify with an increase in AOA as the flow separation becomes more sensitive to the Reynolds number and local wall distortions (37). Hence, deviations in flow behavior, uncertainty, and error in experimental data can be observed. In CFD simulations, such effects can be modeled effectively; to replicate the wind tunnel environment through computation, symmetry boundary conditions are applied to represent walls without increasing the domain (38). For low Reynolds number flows where strain rates are high and flow separation is likely, the turbulence model, the one-equation Spalart-Allmaras model, is preferred because it reduces the production of eddy viscosity (39).

Experiential aerodynamic testing is of utmost importance as it gives information that theory and computer models alone can not fully evaluate, mainly when dealing with complex and practical aerodynamic behaviors. Wind tunnels and measuring instruments like force balances are useful in this process as they are quick, cost-effective, and dependable ways to collect data. Testing is often done together with CFD simulations as experimental results serve to validate and refine computational models and vice versa (40). Some known examples are the Micro Air Vehicle (MAV) developed by ISAE (41), the DLR F-19 model tested at the Low-Speed Wind Tunnel Braunschweig (42), Formula SAE vehicles' university test setup (43), etc.

To get precise aerodynamic data, a fully working force balance is needed, able to measure six inevitable factors, namely drag, lift, side force, and moments for pitching, rolling, and yawing. This force balance must be designed to meet corresponding test-

ing needs, measurement goals, and improvements. Its mechanical and electrical design must be made such that the parts work well together (40). In this regard, strain gauge load cells give precise force measurements by detecting minute deformations in a material when subjected to external loads, thus converting these deformations into electrical signals corresponding to the applied force (44). Then comes the buying of materials, detailed manufacturing, and assembly, all managed properly to make the system accurate and dependable during testing.

CHAPTER 3:
METHODOLOGY

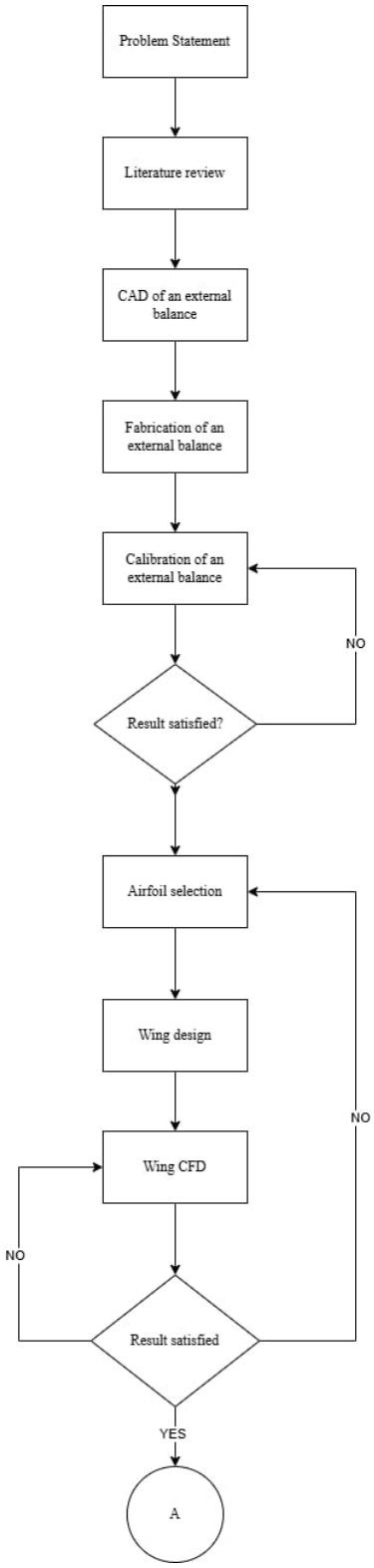

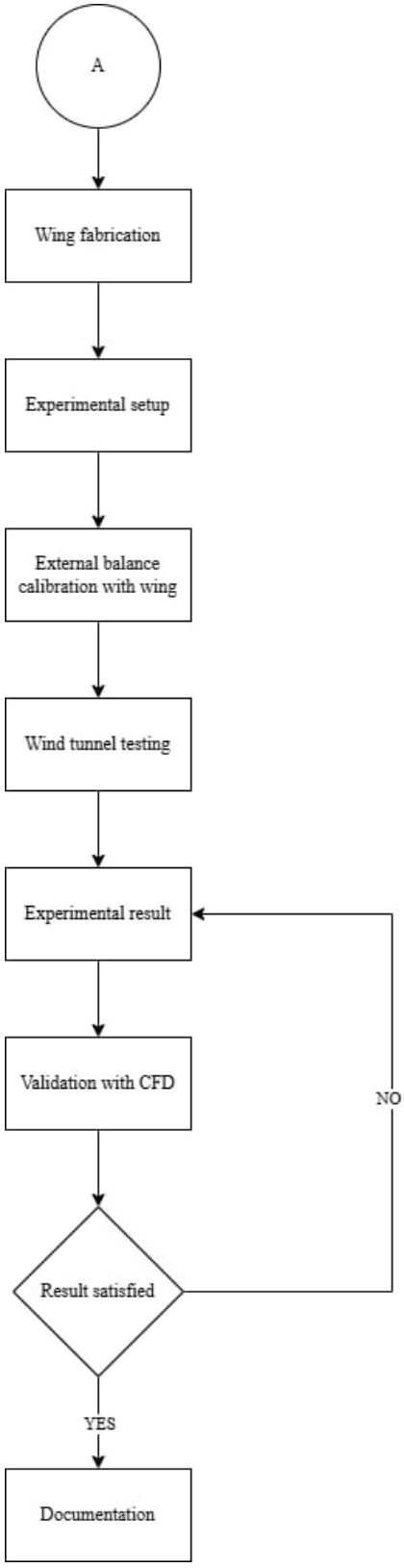

Figure 3.1: Methodology flow chart

3.1 Wing Geometry

Given that humpback whales, massive marine creatures, have unique ridged leading edges on their flippers to maneuver through water despite their size, researchers have long been intrigued by how these irregularities actually benefit rather than hinder performance. Translating this concept into aerodynamics, wing tubercles have been studied extensively for their ability to modify flow characteristics, reduce drag, and improve lift-to-drag.

The present study intends to determine how different tubercle configurations alter aerodynamic efficiency, flow separation behavior, and overall stability. In this regard, the impact of wind tubercles was experimentally studied on external balance performance using a controlled wind tunnel setup. Computational studies shed light on tubercle effects, whereas physical testing validated the theoretical and numerical predictions.

The NACA 63015 airfoil was selected as the baseline, considering its superior stall resistance. Scaled to a chord length of 250 mm, it was imported from Airfoiltools (45) for precise aerodynamic properties. Similarly, to conform to wind tunnel dimensions, the wing was designed with a 250 mm span.

Through literature review and previous wind tunnel studies, the efficacy of NACA 63-series airfoils for experimental applications had been confirmed, which qualifies it for studying the impact of tubercles on flow separation control. Most importantly, the pectoral fins of humpback whales exhibit 15-21% thickness, and to cater to this characteristic, NACA 63015 was chosen for 15% thickness requirement. The airfoil was then extruded in CATIA V5 to generate a 3D wing geometry, serving as the baseline for comparison with tubercled wings, and the very geometry allowed integration of protuberances while sustaining structural integrity for 3D printing and physical testing.

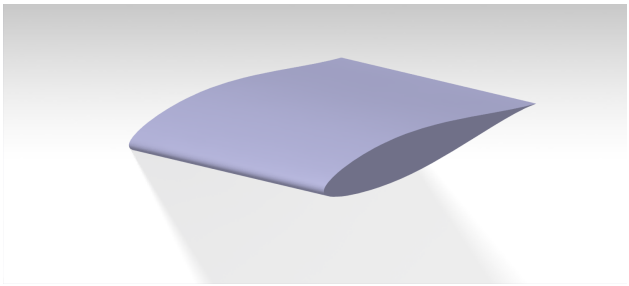

Figure 3.2: Baseline Wing

3.1.1 Tubercle Design Parameters

The wave variation of the wings is dictated by amplitude (A), the vertical displacement of the crests relative to the baseline leading edge and wavelength (λ), and the horizontal distance between two consecutive crests. According to studies, moderate amplitudes generate strong vortex structures that improve lift and stall control, whereas excessive amplitudes may increase drag. Similarly, optimized wavelengths affirm uniform vortex distribution without unnecessary flow disturbances.

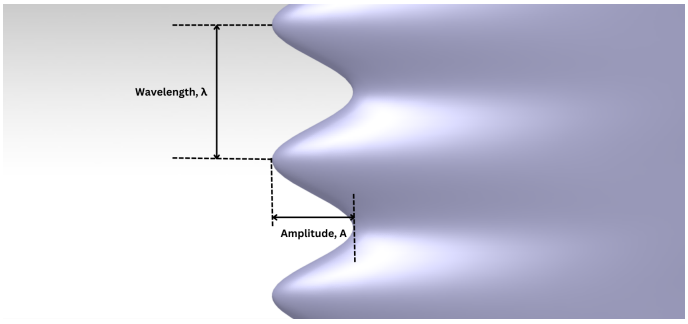

Figure 3.3: Tubercles on the leading edge of a foil

To introduce tubercles, the leading edge of the wing was perturbed by using the sinusoidal function. The sine wave, simply because it resembles most accurately the natural pattern of humpback flippers.

$$y = A\sin(2\pi\, NX) \tag{3.1}$$

Where, A = Amplitude

N = Number of waves

X = Position along the span

While maintaining the airfoil's original shape and aerodynamic characteristics, this equation altered the leading-edge contour. For a smooth transition between the wing body and the tubercles, the redesigned airfoil was then extruded to create a finite 3D wing model in CATIA V-5. Four distinct wing designs were created, each with different wavelength and amplitude combinations. Each configuration had wavelengths of 0.1c and 0.2c with amplitudes of 3% and 6% of the chord, represented by the notation A(x)λ(y).

The specific geometric parameters were:

Table 3.1: Amplitude and wavelength of leading-edge tubercles

Wing	**Amplitude (mm)**	**Wavelength (mm)**
Baseline	-	-
A 7.5 λ 25	3% of chord	0.1 c
A 7.5 λ 50	6% of chord	0.2 c
A 15 λ 25	3% of chord	0.1 c
A 15 λ 50	6% of chord	0.2 c

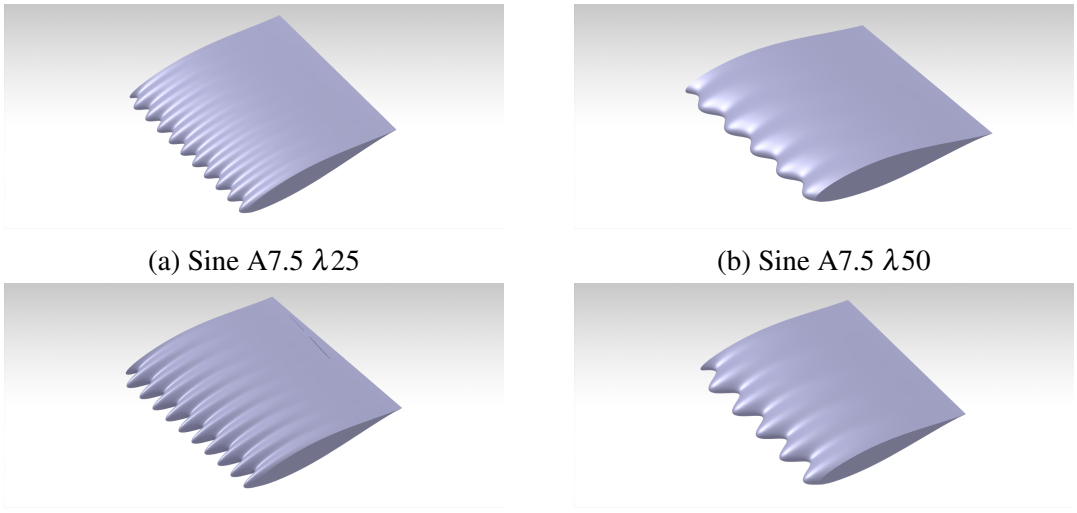

(a) Sine A7.5 λ25

(b) Sine A7.5 λ50

(c) Sine A15 λ25

(d) Sine A15 λ50

Figure 3.4: CAD design of Wing Tubercles

From numerical simulations, it was found that higher amplitudes intensified vortex generation, thus delaying stall. And, shorter wavelengths distributed flow separation control more evenly across the leading edge, whereas longer wavelengths localized the effect. Thus, a 5-pair vs. 10-pair comparison was to examine the effect of varying wavelengths on overall aerodynamic efficiency. Furthermore, the selected amplitude and wavelength values were practical for manufacturing via 3D printing, as extremely small

wavelengths would have introduced fabrication challenges, while excessively high amplitudes might have resulted in structural instability in the wind tunnel.

3.2 Computational Analysis

The fundamental fluid dynamics equation for mass, momentum, and energy conservation using the continuity, momentum, and energy equation governs the CFD simulation. Mass conservation is guaranteed by the continuity equation.

$$\frac{\partial \rho}{\partial t} + \nabla \cdot (\rho \mathbf{u}) = 0 \tag{3.2}$$

Newton's second law provides the momentum equation that guarantees the momentum

$$\rho \left(\frac{\partial \mathbf{u}}{\partial t} + \mathbf{u} \cdot \nabla \mathbf{u} \right) = -\nabla p + \mu \nabla^2 \mathbf{u} + \rho \mathbf{g} \tag{3.3}$$

That said, the computational domain for CFD simulations was designed. The upstream region extended 6 times the chord length, with the wing placed in the XY plane and spanning 125 mm along the positive and negative Z-axis. The side and top walls were put 6 times the chord length away from the wing to minimize boundary effects, and the downstream region was 15 times the chord length to account for reversed flow.

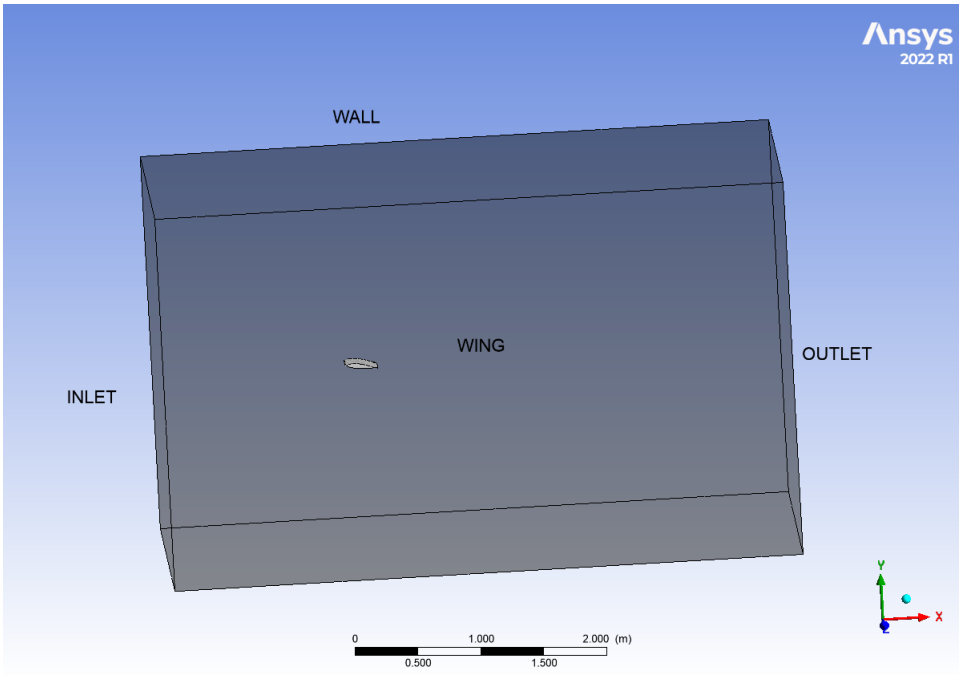

Figure 3.5: CFD Domain

3.2.1 Mesh Generation

With inflation, a 400,000 element mesh was created close to the wing. The inflation had a first layer height of 1e-5 m, 12 layers, and a growth rate of 1.2 was utilized to account for the turbulence impact near wing surface. Since the resulting mesh had $y^+ < 1$, the turbulence effect is considered while ensuring a smooth mesh with face meshing at the wing surface. The 3D tetrahedral structural mesh was employed because it readily accommodates the intricate geometry of leading-edge sinusoidal tubercles and wings. For the mesh to capture the curve of the tubercle, both the capture curvature and capture proximity were applied.

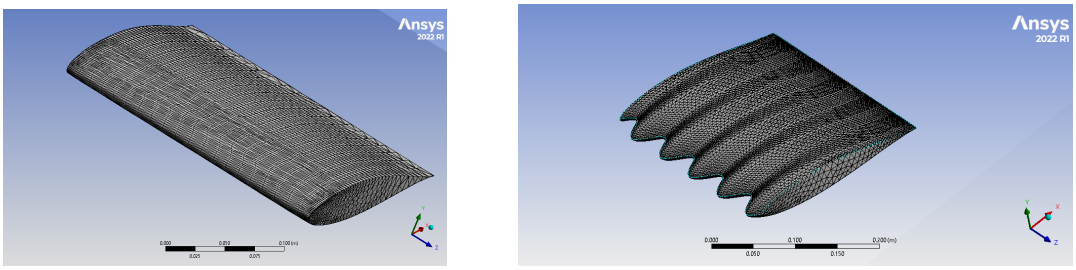

(a) CFD Mesh Baseline Wing (b) CFD Mesh Tubercles Wing

Figure 3.6: Wing Surface Meshes

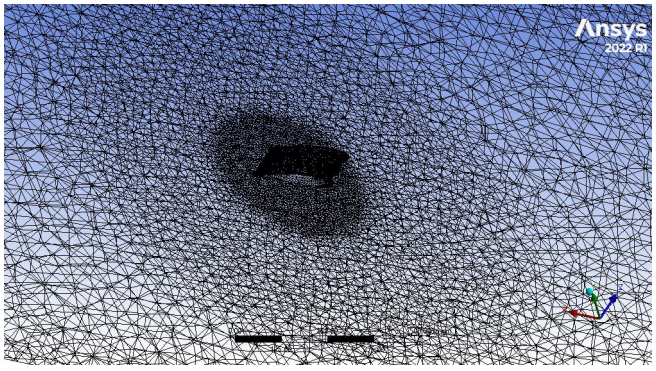

Figure 3.7: Domain Mesh

3.2.2 CFD Setup

The study was conducted at a chord-based low Reynolds number of 85,000. Since the maximum flow from the open wind tunnel was 10 m/s, which is less than Mach 0.3, a pressure-based solver was employed for the computational configuration. Due to boundary layer flow separation at high angles of attack, a transient simulation was used

to capture the fluid's transition from laminar to turbulent.

For turbulence modeling, the four-equation γRe_θ SST model was utilized as it provides better predictions at greater AOA and during flow separation. When examining low-speed flows, the very model is usually employed, being based on the local correlation transition methods.

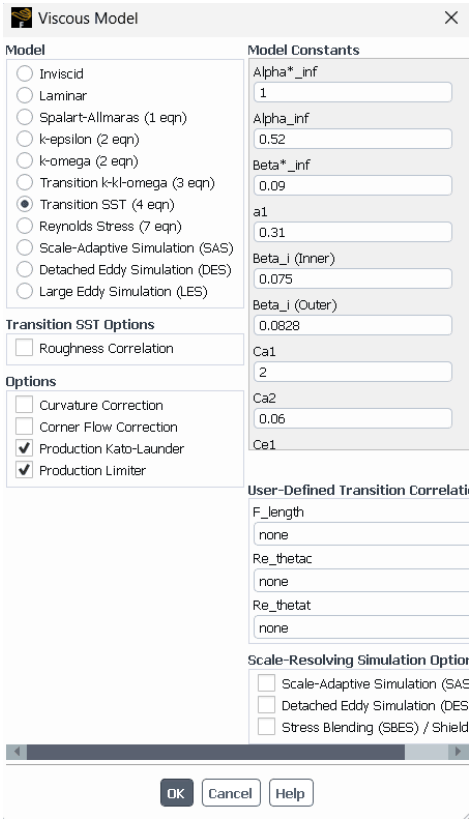

(a) Turbulence model

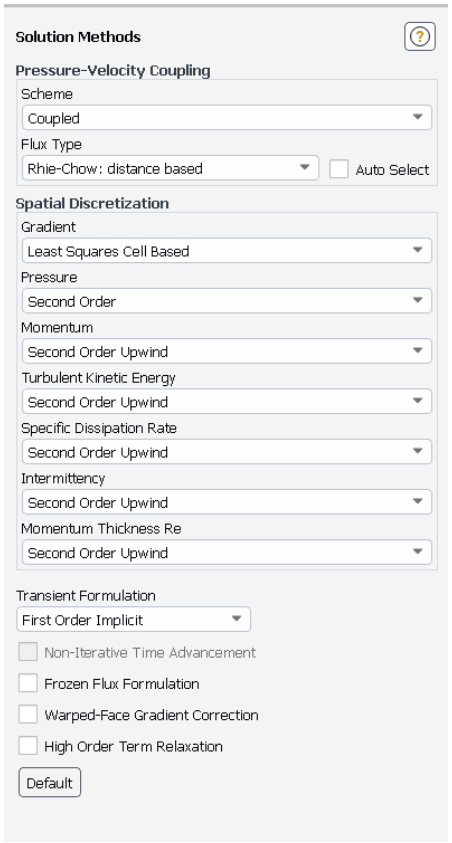

(b) Solver setup

The outlet was given a zero gauge pressure condition, and the wall was treated as a stationary surface with a no-slip boundary condition. The inlet's flow velocity was set at 5 m/s in an axial direction. Specific dissipation rate, intermittency, Turbulent Kinetic Energy, and momentum thickness, all were used to solve the continuity and momentum equation using the COUPLED method, with Second Order pressure discretization and Second Order Upwind schemes for momentum calculations.

Air, with a constant density of 1.225 kg/m^3 and a viscosity of 1.7894e-5 m^2/s, was applied as the working fluid. The C_l and C_d convergence criterion were set to 0.001, whereas the residuals were adjusted to 1e-5 to accommodate for the smooth operation

of the simulation.

Table 3.2: Parameters for CFD analysis

Parameter	**Value**
Solver	Pressure based
Simulation type	Transient
Fluid material	Air
Temperature	280 K
Kinematic Viscosity	1.7896×10^{-5}
Interpolating scheme	Momentum (Second Order Upwind)
	Pressure (Second Order)
	Turbulent Viscosity (Second Order Upwind)
	Momentum thickness
	COUPLED
Turbulence model	$\gamma - Re_\theta$
Inlet velocity	5 m/s
Outlet	0 gauge pressure
Wall	No slip

3.3 Modeling and Fabrication of an External Balance

Many design options are available for measuring the lift and drag forces inside the wind tunnel. For this project, a simple design that cooperates with the wind tunnel was chosen. The dimensions were carefully designed using CATIA based on the specifications of the wind tunnel and its operating conditions. Furthermore, load cells were placed accordingly in the required position for the measurement of aerodynamic forces.

To measure the lift force, a load cell is placed horizontally to detect the vertical deflection caused by the upward force, and conversely, the drag force is measured using a load cell placed vertically to capture the horizontal deflection. The load cells' reaction forces, however, will be computed at a later stage, with a calibration relationship developed to ensure accurate readings. The external balance setup is designed to provide precise force measurements, contributing to a better understanding of the aerodynamic properties of the wing model during wind tunnel testing.

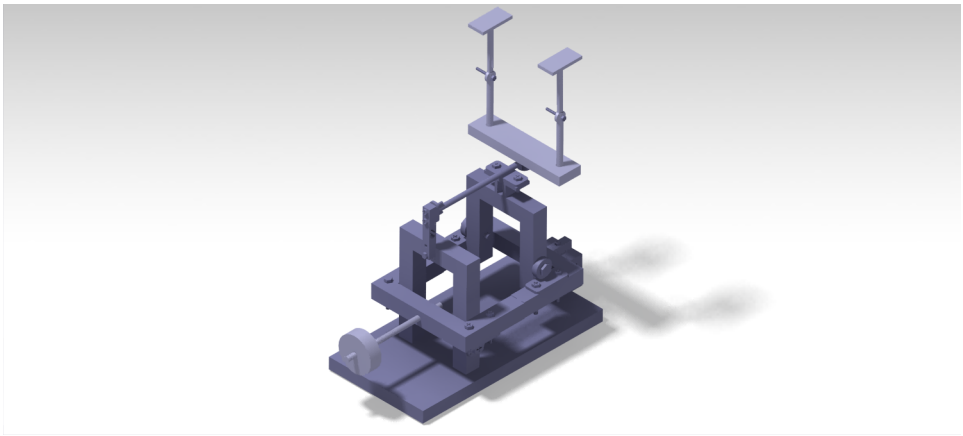

Figure 3.9: CAD Model of an External Balance

The material for the fabrication of an external balance was chosen as PLA+, considering its high strength, ease of manufacturing, and suitability for 3D printing. For instance, PLA+ has high tensile strength (50–70 MPa (46)) and impact resistance, thus is durable under aerodynamic loading conditions. It exhibits low warping and shrinkage during 3d printing, which is essential for the precise fabrication of the balance components with smooth surface finish and rigid structure.

For the assembly, 8 mm threaded rods were used as struts, with a wooden plate as the base plate. This setup becomes a stable, adjustable, and durable structure for the external balance. Two protractors were incorporated for manual adjustments of the angle of attack (AOA) as per the necessity. Finally, a counterweight was added to balance the center of gravity of the system, prevent extra strain on the load cells, and for accurate force measurements.

Figure 3.10: Fabricated External Balance

3.4 Fabrication of Baseline Wing and Tubercled Wings

Since the wings had been designed using CATIA, the CAD model was saved in STL format for facilitating the 3D printing process. The printing material used was again PLA+, a strong and lightweight thermoplastic, and the printing was done using the Bambu Lab 3D printer.

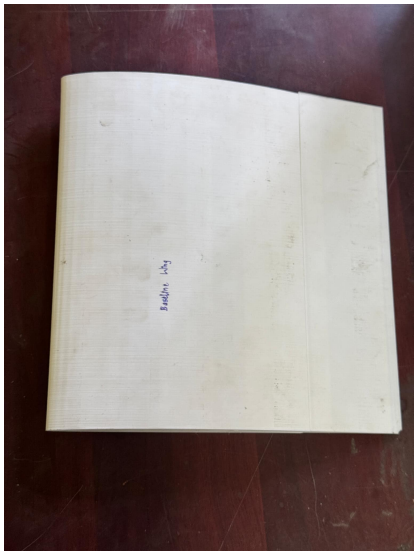

Figure 3.11: Baseline wing

Figure 3.12: A 7.5 λ 25

Figure 3.13: A 7.5 λ 50

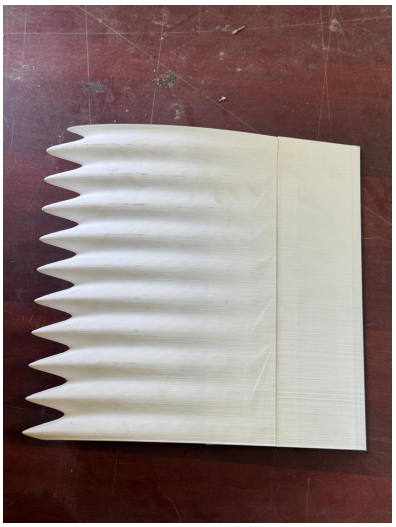

Figure 3.14: A 15 λ 25

Figure 3.15: A 7.5 λ 50

3.5 Experimental Setup

The experimental setup of the project consists of a precisely calibrated and arranged wind tunnel and external balance system that measures the aerodynamic loads, like lift and drag, acting on a wing model. The balance system is placed inside the subsonic wind tunnel for measuring force, and a tubercles wing model is mounted for testing at different angles of attack (AOA). The system, firmly mounted to the base of the test section with nuts and bolts, ensures its stability and rigidity throughout the experiment. This configuration minimizes movement or instability that could compromise measurement accuracy.

The test model is fixed to the two vertical struts of the external balance. Protractors helped adjust AOA, whereas its corresponding rotating mechanism aids controlled variation in angles.

Figure 3.16: Experimental setup

The external balance is equipped with separate lift and drag load cells for force measurement. These load cells are connected to the HX711 amplifiers, which are further connected to Arduino Uno. The signals from the amplifier are sent to Arduino Uno,

where the data is processed, and the output result is displayed in the serial monitor of the Arduino Integrated Development Environment (IDE).

For maintaining consistency in the experimental conditions, the wind tunnel was set to operate at a constant airflow speed of about 5 m/s, which is the specific condition for the experiment. An anemometer was used to check the airflow speed around the test model to ensure that the flow at the test model was at around 5 m/s, which was the flow required for the experiment.

Figure 3.17: Velocity check via Anemometer

3.6 External Balance Calibration

To accurately estimate lift and drag forces acting on a test model inside the wind tunnel, the external balance is calibrated. The calibration process establishes a relationship between the output signals from the strain gauge load cells and the applied forces. Specific calibration steps are done individually for the lift and drag load cells by applying known weights.

The external balance is calibrated to measure lift and drag forces accurately in a wind tunnel experiment. Due to structural interactions, cross-talk effects occur, where lift influences drag measurements and vice versa. To address this, a calibration process is conducted for both load cells, followed by an analysis of cross-talk effects, leading to the formulation of correction equations.

Due to the effect of the structure of the external balance, readings observed in load cells encased contributions from the balance itself. Nonetheless, to ensure accurate force measurements, an experimental setup of the external balance, excluding the wing, was placed in the wind tunnel, and lift and drag were measured at approx. 5 m/s. Repeating for tens of times, the mean values of lift and drag were found to be 0.24 N and 0.28 N, respectively. These values were later subtracted from the final readings to account for the additional forces introduced by the balance structure.

3.6.1 Calibration of the Lift Load Cell

To determine the correlation between the load cell output and known applied forces in the lift direction.
Procedure for calibration of the lift load cell:

- The external balance was set up on a stable platform to minimize vibrations.
- The lift load cell was connected to the HX711 amplifier and interfaced with an Arduino Uno for data acquisition.
- A known weight was placed vertically to the test section, and the known value was given as input for calibration. Thereafter, the weight was removed to check the zero reading of the lift load cell when no load was applied to it.
- When zero reading was achieved after removing the initial known weight, then different known weights were placed incrementally above the test section to apply a vertical force.
- The corresponding output data from the lift load cell were recorded for each applied weight.

- The procedure was repeated multiple times to ensure consistency and minimize errors.

(a) Front view (b) Back view

Figure 3.18: Calibration of lift load cell

3.6.2 Calibration of the Drag Load Cell

To determine the correlation between the load cell output and known applied forces in the drag direction.

Procedure for calibration of the drag load cell:

- The external balance was set up on a stable platform to minimize vibrations.
- The drag load cell was securely mounted and aligned to accurately measure horizontal forces.
- The drag load cell was connected to the HX711 amplifier and interfaced with an Arduino Uno for data acquisition.
- A rope was connected to the test section, aligned with the drag direction resembling the pulley mechanism.
- A known weight was hung vertically to the rope connecting the test section, and the value of the known weight was given as input for calibration. Then the weight

was removed to check the zero reading of the drag load cell when no load is applied to it.

- A series of known weights was attached to the rope, hanging at a fixed distance to generate a controlled horizontal force.
- The corresponding output data from the drag load cell was recorded for each applied weight.
- The procedure was repeated multiple times to ensure consistency and minimize errors.

Figure 3.19: Calibration of drag load cell

3.6.3 Cross-Talk Effect Analysis and Correction

During calibration, it was observed that applying a pure lift force also affected the drag readings and vice versa. This error in calibration is known as cross-talk effect, and it must be addressed in order to obtain proper readings from the load cells.

In order to minimize this effect, the following steps were taken:

- A known lift force was applied while monitoring changes in drag readings.
- A known drag force was applied while monitoring changes in lift readings.
- Multiple trials were conducted for different weight values to establish a trend.
- Based on the observed cross-talk effects, equations were derived to compensate for the influence of lift on drag and drag on lift.
- These correction matrices for lift and drag are expressed as:

$$\begin{bmatrix} A \\ B \end{bmatrix} = \begin{bmatrix} -0.4644 & 1 \\ -0.65441 & 1 \end{bmatrix} \begin{bmatrix} X \\ Y \end{bmatrix} + \begin{bmatrix} 5.20148 \\ -5.30672 \end{bmatrix}$$

- These correction equations were applied to all experimental data to ensure accurate force measurements.

3.7 Data Collection and Analysis

The two load cells attached to the external balance are used to obtain the resulting lift and drag forces acting on the wing model. The load cells are connected to the HX711 amplifier where the excitation wires (red and black) are connected to the E+ and E- pins respectively, whereas the signal wires (white and green) are connected to the A+ and A- pins of the HX711 amplifier respectively.

Similarly, the HX711 amplifier is then connected to the Arduino Uno, where VCC is connected to the 5V pin, GND is connected to the GND pin,, and finally, the data (DT) and clock (SCK) pins are connected to the digital pins, pin 2 and pin 3, respectively.

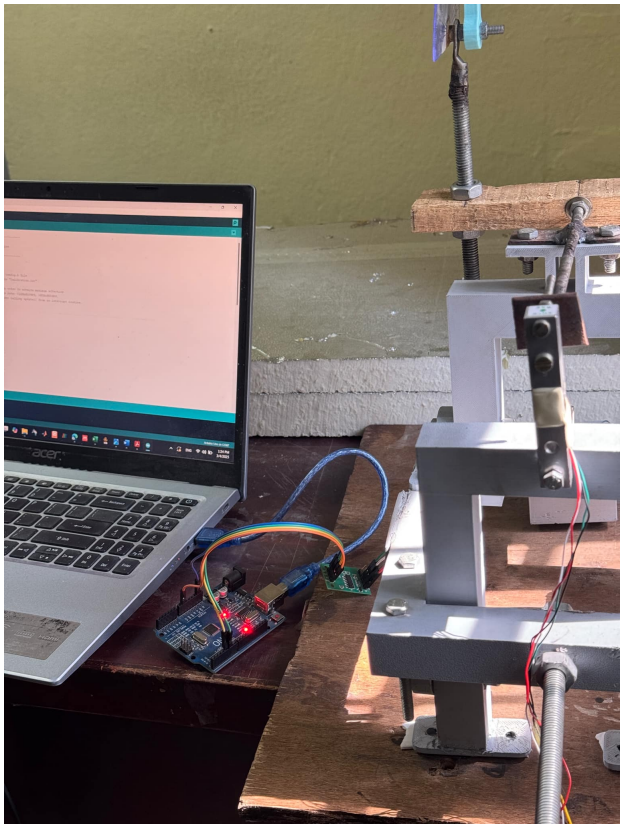

Figure 3.20: Connection of load cell, HX711 and Arduino Uno

The data from the load cells are processed by the Arduino Uno, which reads the signals from the HX711 amplifier. The HX711 library is used by the Arduino code to convert an analog signal from the load cells into digital values. The corresponding digital lift and drag forces acting on the wing model are calculated and displayed on the Arduino IDE's serial monitor in real time. During the experiment, the wind speed was kept constant at 5 m/s, and the output was displayed on the serial monitor. The output values were measured continuously about the AoA of the wing where lift and drag force were measured at various angles.

The experiment was repeated 10 times for each angle of attack to get more precise and accurate results. Then, the obtained data was further refined using the correction equation obtained from the correction factor of the external balance due to cross-talk error during calibration. The finally obtained resultant lift and drag forces were plotted to examine the aerodynamic characteristic of the tubercles wings. The effect of using leading edge wing tubercles was seen by plotting the obtained resultant lift and drag at the same angle of attacks for both tubercles and the baseline wing.

CHAPTER 4:
RESULT AND DISCUSSION

4.1 Experimental Findings

The two non-dimensional parameters for the study of wings are the coefficient of lift

$$C_l = \frac{L}{\frac{1}{2}\rho V^2 S} \tag{4.1}$$

and the coefficient of drag

$$C_d = \frac{D}{\frac{1}{2}\rho V^2 S} \tag{4.2}$$

where ρ is density, V is velocity, and S is the reference area. The experimental data of baseline and tubercle wings at various angles of attack are shown in the graph (Figure 4.1). It illustrates the impact of employing leading-edge wing tubercles. Up to 16 °, the baseline wing's C_l grows steadily as the angle of attack rises; after that, it decreases, signifying the wing's stall.

The leading-edge tubercles with A7.5λ50 produced the best results by showcasing a progressive increase in C_l with increasing angles of attack and delaying the stall by up to 24° compared to the baseline wing and rest of the tubercled winds. On the other hand, A15λ50 wing yielded moderate results, delaying the stall by up to 20 ° and a similar rise in C_l at a greater angles of attack. The other tubercle wings (A7.5λ25, and A15λ25) performed poorly, exhibiting early stall and lower C_l values. The A15λ25 wing had a higher flow resistance due to the shorter wavelength and larger amplitude, which led to early flow separation.

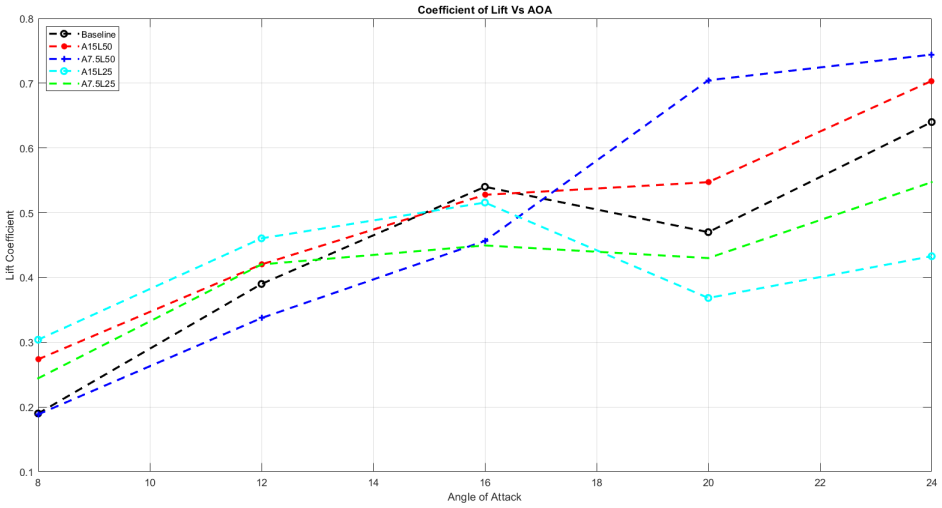

Figure 4.1: Coefficient of Lift vs AOA

The best results were obtained by the tubercles wing with a high wavelength and low amplitude by improving C_l and delaying the stall by almost 6° with the generation of strong vortices at the trough zone. Beyond the baseline wing's stall angle, the A7.5λ50 tubercles increased the lift coefficient by an impressive 17%.

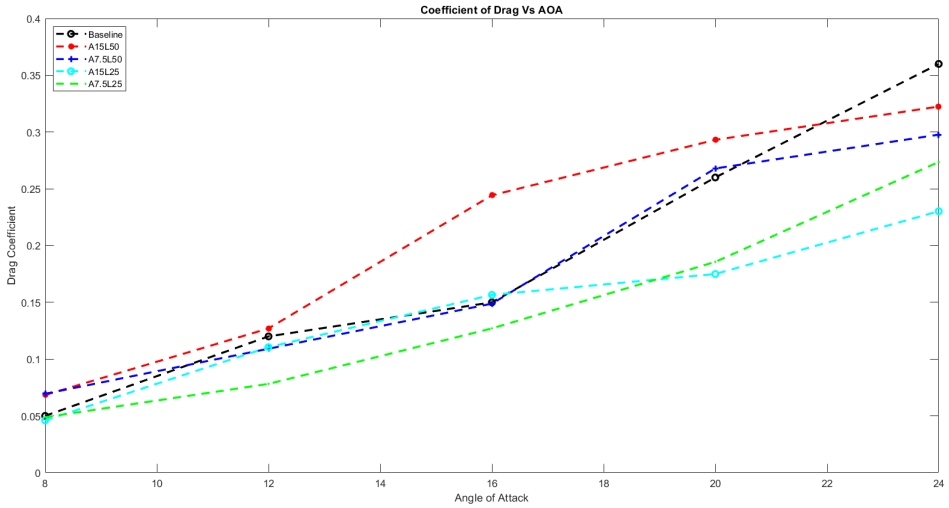

Figure 4.2: Coefficient of Drag vs AOA

These findings propose that although tubercles can increase lift and delay stall, their efficacy depends on certain design factors, say wavelength and amplitude. Considering the drag coefficient graph, drag rises with the angle of attack, and after 16°, the baseline wing experiences a sharp rise in drag, signifying flow separation and stall. The A7.5λ50 wing exhibits a pattern that is comparable to the baseline wing but with

higher drag, meaning that higher wavelength tubercles cause more drag. Conversely, the shorter wavelengths provide less drag than the baseline wing.

Moreover, large-wavelength tubercles create a powerful leading-edge vortex that increases lift but also raises drag because of more turbulent mixing at higher angles of attack. Since a weaker vortex is created by the shorter wavelength, there is less turbulent mixing, hence, the reduced overall. In this regard, the A7.5λ50 tubercle configuration, which has the highest aerodynamic efficiency, reduces drag by 12%.

Table 4.1: Aerodynamic Measurements for Different Wings at Various AOAs

AOA	**Baseline**		**A7.5 λ50**		**A15 λ50**		**A7.5 λ25**		**A15 λ25**	
	c_l	c_d	c_l	c_d	c_l	c_d	c_l	c_d	c_l	c_d
8	0.19	0.05	0.18	0.07	0.27	0.07	0.24	0.05	0.30	0.04
12	0.39	0.12	0.33	0.11	0.42	0.127	0.42	0.08	0.46	0.11
16	0.54	0.15	0.45	0.15	0.52	0.244	0.45	0.127	0.51	0.156
20	0.47	0.26	0.70	0.27	0.54	0.293	0.43	0.185	0.36	0.175
24	0.64	0.36	0.74	0.30	0.70	0.322	0.54	0.273	0.43	0.23

The baseline wing graph shows a decline in the C_l/C_d ratio beyond 16°, indicating that drag increases faster than lift. The A7.5λ50 tubercle wing, however, exhibits a higher C_l/C_d ratio, suggesting improved efficiency at lower angles of attack. The graph also shows that a larger amplitude results in higher drag due to increased vortex strength.

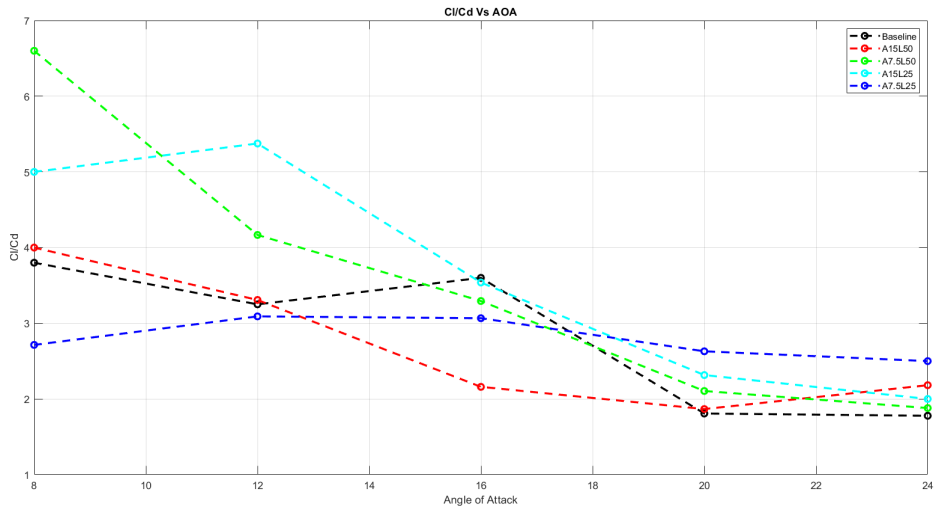

Figure 4.3: Cl/Cd vs AoA from experiment

To ensure that the convergence of the results is independent of the mesh element that was generated, a grid independence test was conducted. The figure illustrates that when the element surpasses approximately 0.45 million, the performance parameter for the tubercle wing remains unchanged. When simulating the NACA 63215 baseline and tubercles wing, a mesh of 0.45 million elements was utilized as the standard parameter because increasing the number of elements lengthens the computation time.

Here, both the C_l and C_d begin to stabilize as the mesh density increases past this point, means the solution is no longer influenced substantially by further grid refinement. C_l values plateau near 0.424, while C_d values level off around 0.080, confirming that the selected mesh is sufficient for capturing the aerodynamic behavior with consistency. Using a mesh that balances accuracy and computational efficiency is crucial for CFD results to remain valid without introducing unnecessary computational cost. Moreover, conducting this GIT built confidence in the reliability of the simulation outcomes and eliminated concerns about mesh-induced errors. The selected mesh was used throughout to observe performance across various AOA without compromising the accuracy or stability of the solution.

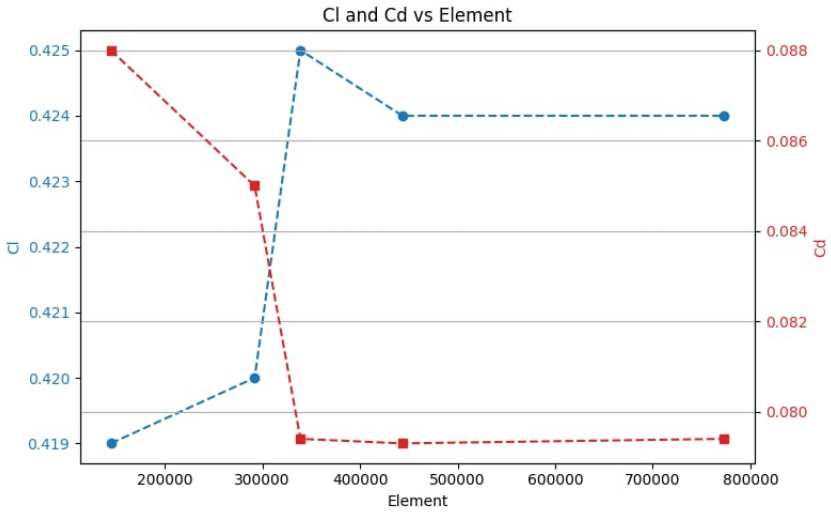

Figure 4.4: Grid Independence Test

The experimental data and computational analysis of the tubercles leading-edge wing compared to the baseline NACA 63215 wing show similar trends in the coefficient of lift and coefficient of drag across pre-stall, stall, and post-stall zones.

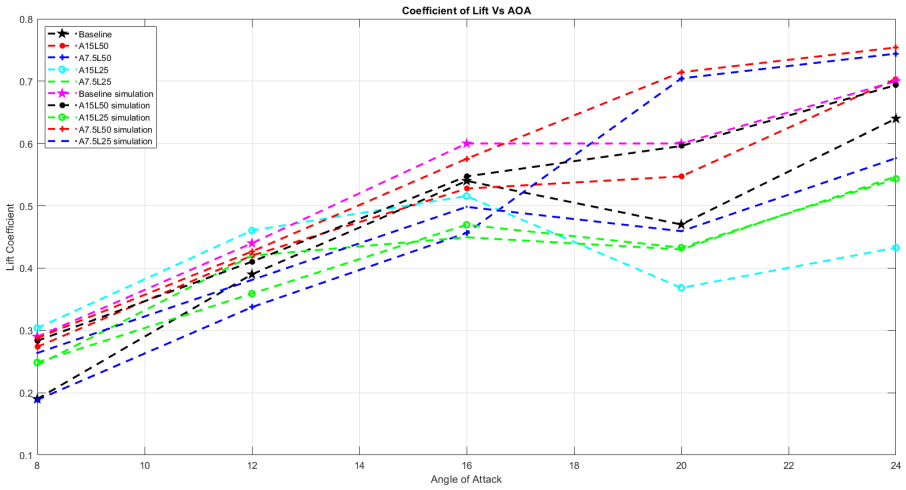

(a) Coefficient of Lift vs AOA

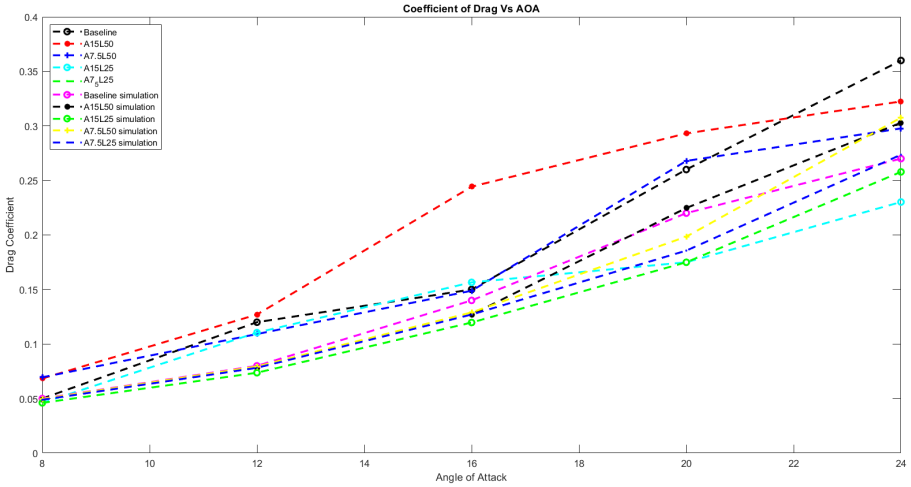

(b) Coefficient of Drag vs AOA

Figure 4.5: Comparison of Experimental Data with CFD Data

4.2 Computational Outcomes

4.2.1 Pressure Distribution

At 20° angle of attack, the baseline wing exhibits a notable divergence of flow at the trailing edge, which denotes the flow separation. The uneven streamlines confirm unstable flow behavior, meanwhile, high-pressure regions near the stall's leading edge highlight the onset of the stall. Lower flow attachment under those circumstances results from the baseline wing's inability to regulate vortex formation due to its smooth leading edge without alteration.

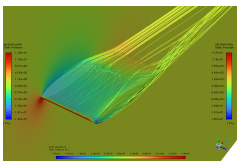

(a) 8° AOA

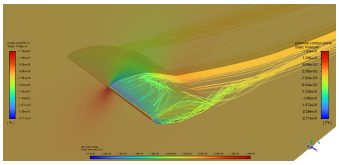

(b) 12° AOA

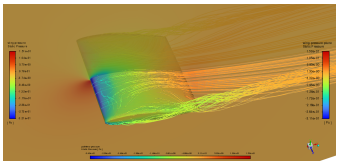

(c) 16° AOA

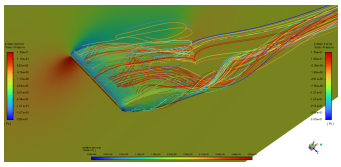

(d) 20° AOA

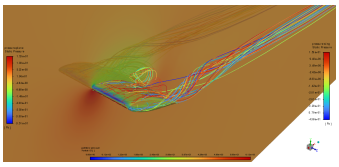

(e) 24° AOA

Figure 4.6: Pressure Distribution for Baseline Wing

Alternatively, the streamlined and well-organized airflow in the mid- and outboard areas is demonstrated by the tubercle structure. The presence of tubercles generates localized flow variations, thereby forming smaller vortices along the leading edge. This energizes the boundary layer by improving flow attachment and aiding to a smoother pressure distribution across the surface.

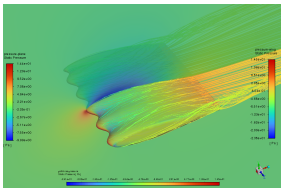

(a) 8° AOA

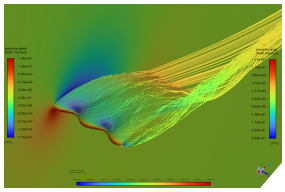

(b) 12° AOA

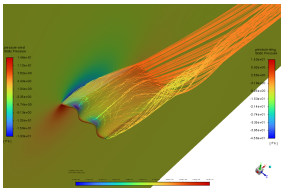

(c) 16° AOA

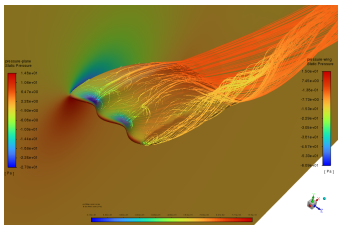

(d) 20° AOA

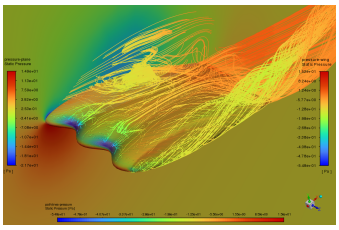

(e) 24° AOA

Figure 4.7: Pressure Distribution for A7.5λ50 Tubercles Wing

4.2.2 Velocity Distribution

In the baseline wing, flow is smoothly accelerated by the leading edge but starts to split apart as it approaches the trailing edge. Due to low energy, which increases aerodynamic drag, it displays a chaotic velocity streamline at 20° AOA, indicating both flow separation and recirculation.

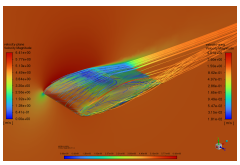

(a) 8° AOA

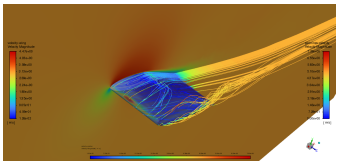

(b) 12° AOA

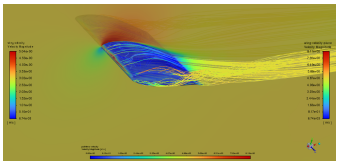

(c) 16° AOA

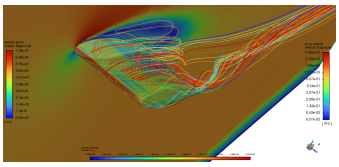

(d) 20° AOA

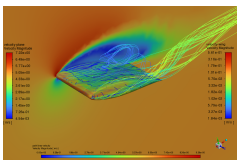

(e) 24° AOA

Figure 4.8: Velocity Distribution for Baseline Wing

The very distribution is changed by the tubercle pattern by replacing large-scale flow separation with multiple smaller vortices along the leading edge. The vortices help re-energize the flow, resulting in smoother, more organized streamlines and reduced flow disturbance.

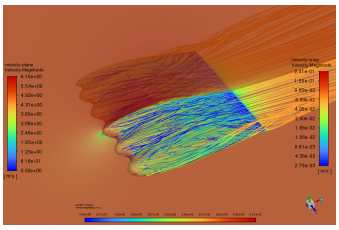

(a) 8° AOA

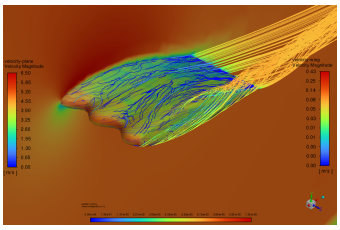

(b) 12° AOA

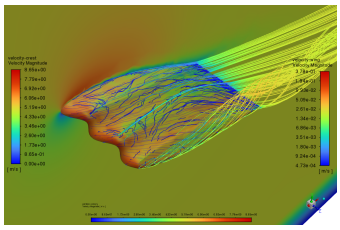

(c) 16° AOA

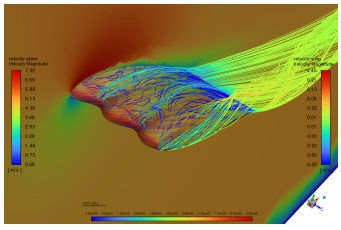

(d) 20° AOA

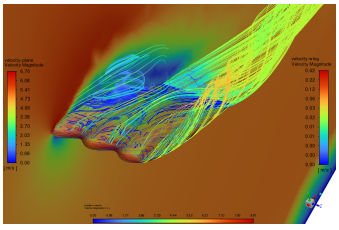

(e) 24° AOA

Figure 4.9: Velocity Distribution for A7.5λ50 Tubercles Wing

4.2.3 Turbulence Kinetic Energy

At 20° AOA, the baseline wing has low Turbulent Kinetic Energy close to the leading edge, which means there is smoother flow according to the turbulence kinetic energy contour. However, the turbulence increases toward the trailing edge due to flow separation with strong turbulence dissipation beyond the wing surface, which lowers

efficiency.

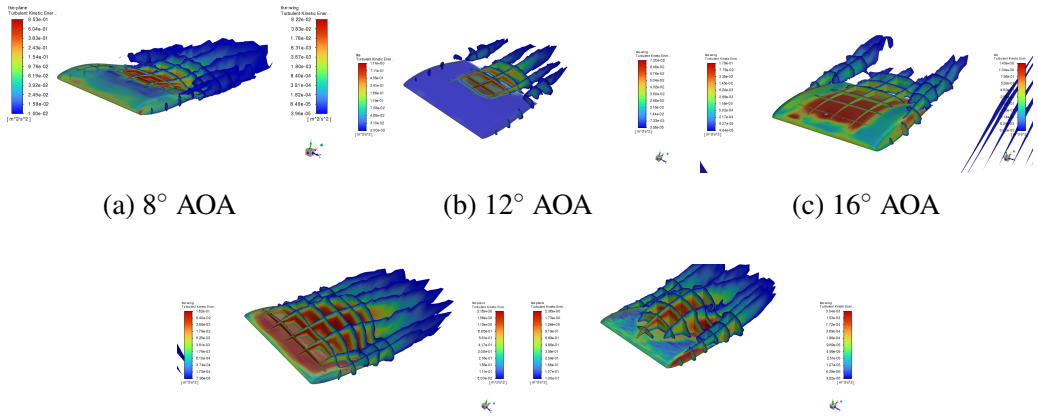

(a) 8° AOA (b) 12° AOA (c) 16° AOA

(d) 20° AOA (e) 24° AOA

Figure 4.10: Turbulence Kinetic Energy for Baseline Wing

Given that tubercles regulate flow separation and delay stall, the TKE contour for the tubercles arrangement at 20 ° AOA shows less turbulence intensity, indicating attached flow and more localized turbulence. By intending to keep flow linked longer before detaching the surface, lower aerodynamic losses and improved efficiency will be acquired due to less energetic turbulence.

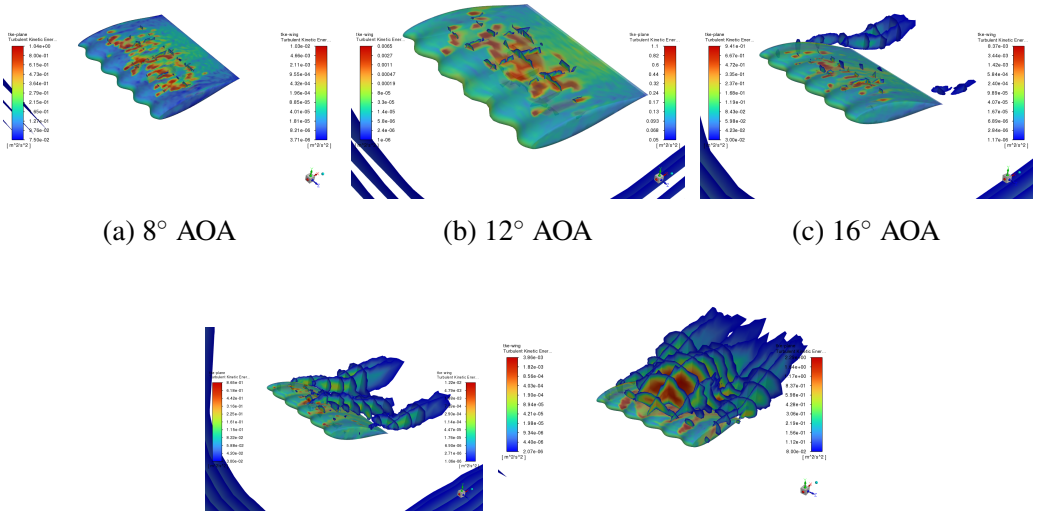

(a) 8° AOA (b) 12° AOA (c) 16° AOA

(d) 20° AOA (e) 24° AOA

Figure 4.11: Turbulence Kinetic Energy for A7.5λ50 Tubercles Wing

While the tubercles wing seems to lessen turbulence and regulate the strong vortex shedding, the baseline wing experiences more turbulence and higher energy dissipation, which results in more drag.

4.2.4 Vorticity Distribution

The flow separation is delayed by the counter-rotating vortex created by tubercles, which re-energizes the boundary layer flow connection—the localized pressure variation produced by the vortex shape aids in the more even distribution of lift. The wake from the baseline wing is characterized by large-scale vortex shedding due to its uniform vorticity distribution and broad area of flow separation.

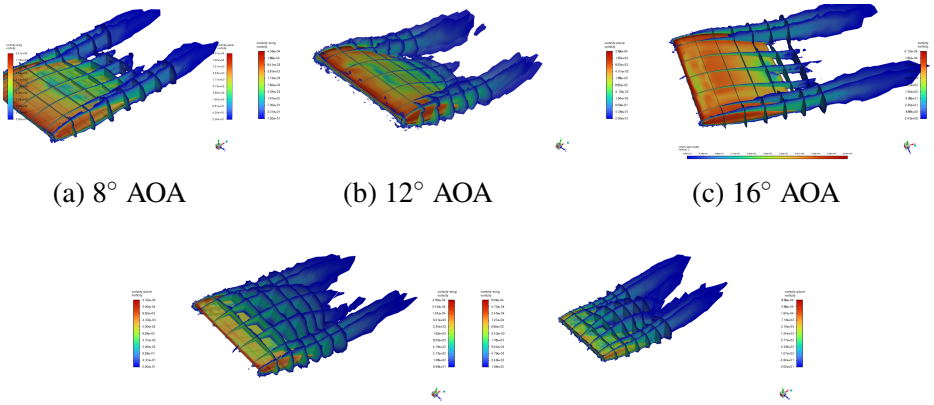

(a) 8° AOA (b) 12° AOA (c) 16° AOA

(d) 20° AOA (e) 24° AOA

Figure 4.12: Vorticity Distribution for Baseline Wing

Tubercle wings have a distinct vortex shape that suggests a counter-rotating vortex has been formed. The organized wake produced by the tubercles suggests that the vortices, which are concentrated locally behind the tubercles, effectively manage flow separation.

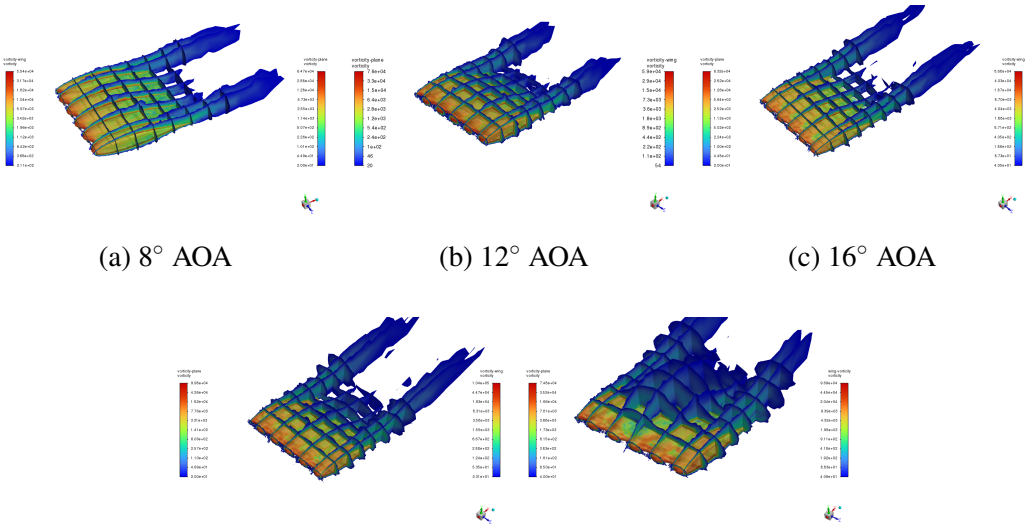

(a) 8° AOA (b) 12° AOA (c) 16° AOA

(d) 20° AOA (e) 24° AOA

Figure 4.13: Vorticity Distribution for A7.5λ50 Tubercles Wing

4.2.5 Aerodynamic Performance of Tubercled Wings Across Stall Regimes

Pre-Stall Region (8 - 16°)

→ Minor separation in the trough was observed, indicating early flow instability.

→ Moderate tubercle-induced KE generation occurred due to mild vortex formation, which helped in maintaining flow attachment.

→ Lift improvement was noted due to the enhanced boundary layer energy, improving aerodynamic efficiency.

→ A slight increase in drag was observed, primarily due to increased pressure drag as flow attachment was delayed but not fully stabilized.

Near Stall Region (16 - 20°)

→ Increased separation occurred in the tubercle trough, with flow becoming more turbulent in this region.

→ High KE generation from the tubercles was observed due to strong vortex formation.

→ Strong streamwise vortices formed along the tubercle ridges, increasing momentum mixing and maintaining boundary layer attachment.

→ Lift was sustained for a longer period compared to the bare wing due to vortex-induced flow reattachment in regions where separation would typically occur.

→ Drag increased due to the higher wake turbulence and the recirculation zone formed in the boundary layer, leading to higher pressure drag.

Post-Stall Region (20 - 24°)

→ Large-scale separation occurred over most of the wing, affecting the overall aerodynamic performance.

→ Tubercle-induced KE decreased in the attached regions but remained high in the wake, indicating a persistence of vortex activity downstream.

→ Lift dropped, but the decline was more gradual compared to the straight wing, as flow reattachment was less abrupt.

→ A further increase in drag was noted due to the large-scale flow separation and increased turbulent wake.

4.2.6 Flow Visualization

Smoke Visualization

The flow visualization streamline and the computational analysis streamline at 24° angle of attack for baseline wing and tubercles wing represents the flow separation. The flow separation and flow recirculation can be visualized using smoke visualization.

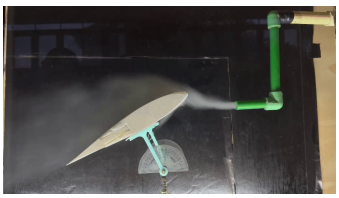

(a) baseline

(b) A7.5λ50

(c) A15λ50

(d) A15λ25

(e) A7.5λ25

Figure 4.14: Smoke Visualization of Wing Tubercles at 24° AOA

Tuft Visualization

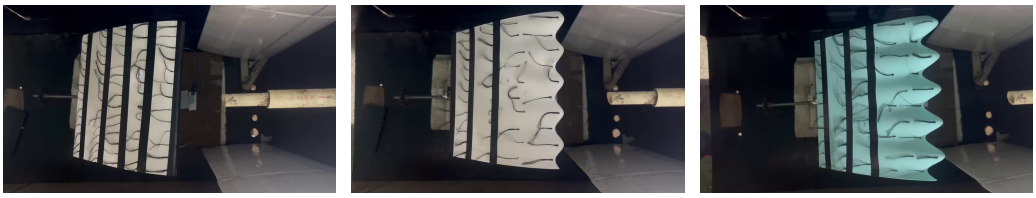

(a) baseline (b) A7.5λ50 (c) A15λ50

(d) A7.5λ25 (e) A15λ25

Figure 4.15: Tuft Visualization of Wing Tubercles at 24° AOA

4.3 Limitations of the Project

- Cross-talk between sensors affects the accuracy of force measurements in certain test configurations.
- Manual adjustment of the angle of attack limits the precision of measurements and introduces human errors.
- Aligning the wing with the struts is quite arduous, and probable misalignment can affect aerodynamic results.
- A single Arduino could have been used to handle both lift and drag measurements from the load cells.
- The project is limited to testing the aerodynamic behavior of wings without considering long-term performance factors like material fatigue.
- The fabrication process is constrained by the resolution of the 3D printer, which might have affected the accuracy of the tubercle geometry to some extent.

4.4 Problems Faced

Some of the challenges encountered during the project are summarized below:

- Structural vibrations interfered with load cell calibration and caused fluctuations in force measurements.
- Memory constraints during CFD simulations slowed down processing and led to crashes.
- Fabricating precise sinusoidal wave tubercles was challenging.
- The limited build area of the 3D printer required printing the wing section-wise.
- Measuring aerodynamic forces at high angles of attack became difficult due to flow separation and instability.
- Large data from experiments and CFD simulations made analysis complex and time-consuming.
- Amplifier malfunctions resulted in incorrect readings and hindered the calibration process.
- Maintaining a precise wind speed of 5 m/s in the tunnel was difficult, given the flow inconsistencies.

CHAPTER 5:
CONCLUSION AND FUTURE ENHANCEMENT

5.1 Conclusion

According to the research, employing the tubercle protuberances near the wings' leading edge causes lift to increase and stall to delay at low Reynolds numbers. When compared to the baseline wing's stall zone, the leading-edge tubercles postpone stall by 6°, increase lift by 17%, and reduce drag by 12%. The creation of a vortex in the trough region and a significant adverse pressure gradient behind the trough aid this stall delay. As a result of the tubercles forming a compartmentalized flow structure along the wing span, the flow in one compartment is unaffected by the stalling of another.

Among numerous configurations that could be generated by varying wavelength and amplitude, the leading-edge tubercles with an amplitude of 3% chord and a wavelength of 20% chord produce more lift than the baseline wing at the pre-stall, stall, and post-stall zones. As per the drag coefficient plot, the drag increases as the angle of attack increases. The tubercle configuration A7.5λ50 shows a drag plot similar to the baseline wing, suggesting that the smaller amplitude and larger wavelength improve the aerodynamic efficiency by reducing flow resistance.

All things considered, it can be said that the tubercles' leading edge improves aerodynamic efficiency and delays stall. The study concludes that a tubercle wing with a wavelength of 0.2c and an amplitude of 3% of chord have better aerodynamic behavior under cruising and moderate angle of attack conditions than other configurations of tubercles and baseline wing.

5.2 Scope for Future Work

- The experiment was conducted at a constant wind speed of 5 m/s. Future studies could explore varying speeds to examine the effects of Reynolds number on leading edge wing tubercles.
- Pressure taps could be added along the wing surface with pressure sensors to get more detailed insights into flow behavior and pressure distribution.
- A servo motor mechanism can be implemented instead of manually adjusting the AoA using protractor.
- Future research could focus on testing leading edge wing tubercles on a scaled down UAVs or robotic aircraft under real flight condition to evaluate their practical benefits.
- Testing of different tubercles wing designs, such as swept wings, can be done to analyze how tubercles dictate aerodynamic efficiency in various configurations.

BIBLIOGRAPHY

[1] J. Barlow, W. Rae, and A. Pope, *Low-Speed Wind Tunnel Testing*. Wiley, 1999. [Online]. Available: https://books.google.com.np/books?id=nUHWDwAAQBAJ

[2] "Design and development of a subsonic wind tunnel with a gust generator featuring oscillating vanes for enhanced flow visualization."

[3] D. Trent, "load cell:high quality load cell and force sensors." [Online]. Available: https://www.800loadcel.com/

[4] K. Gore, A. Gote, A. Govale, A. Kanawade, and S. Humane, "Aerodynamic analysis of aircraft wings using CFD," vol. 05, no. 6.

[5] S. Post and M. Morris, "Force balance design for educational wind tunnels," in *ASEE Annual Conference & Exposition*. American Society for Engineering Education, 2010, pp. 15–594.

[6] B. Johnson, "NACA 4412 low reynolds number aerodynamic performance," publisher: Unpublished. [Online]. Available: https://rgdoi.net/10.13140/RG.2.2.34127.36000

[7] D. S. Miklosovic, M. M. Murray, and L. E. Howle, "Experimental evaluation of sinusoidal leading edges," *Journal of Aircraft*, vol. 44, no. 4, pp. 1404–1408, 2007.

[8] A. Sharma, R. Singh, and P. Kumar, "Effects of leading-edge tubercles and dimples on a cambered airfoil and its performance," *International Research Journal of Engineering and Technology*, vol. 9, no. 4, pp. 1185–1190, 2022. [Online]. Available: https://www.irjet.net/archives/V9/i4/IRJET-V9I4195.pdf

[9] D. S. Miklosovic, M. M. Murray, L. E. Howle, and F. E. Fish, "Leading-edge tubercles delay stall on humpback whale (megaptera novaeangliae) flippers," *Physics of Fluids*, vol. 16, no. 5, pp. L39–L42, 2004.

[10] T. Banu and J. Karthikeyan, "Optimization of tubercle wing," *Journal of Cardiovascular Disease Research*, vol. 12, no. 7, pp. 2121–2122, 2021.

[11] M. B. Anwar, A. Shahzad, and N. M. Qadri, "Effects of leading-edge tubercles on the aerodynamic performance of wings," in *MDSRIC - 2019 Proceedings*. Wah, Pakistan: Department of Aerospace Engineering, College of Aeronautical Engineering, National University of Sciences and Technology, Pakistan, November 2019.

[12] Z. Wei, T. H. New, and Y. D. Cui, "An experimental study on flow separation control of hydrofoils with leading-edge tubercles at low reynolds number," *Ocean Engineering*, vol. 108, pp. 336–349, 2015. [Online]. Available: https://daneshyari.com/article/preview/8065422.pdf

[13] J. Zhang, S. Liu, Q. Yan, B. C. Khoo, C. Liu, M. Guo, and W. Wei, "Numerical and experimental analysis of biomimetic tubercle for cavitation suppression in viscous oil flow around hydrofoil," *Engineering Applications of Computational*

Fluid Mechanics, vol. 18, no. 1, p. 2394176, Dec. 2024. [Online]. Available: https://www.tandfonline.com/doi/full/10.1080/19942060.2024.2394176

[14] P. Watts, "THE INFLUENCE OF PASSIVE, LEADING EDGE TUBERCLES ON WING PERFORMANCE."

[15] R. Bhaskaran and L. Collins, "Introduction to CFD basics."

[16] M. Gonzalez, J. M. Ezquerro, V. Lapuerta, A. Laverón, and J. Rodríguez, "Components of a wind tunnel balance: Design and calibration," *Wind Tunnels and Experimental Fluid Dynamics Research*, pp. 1–20, 2011.

[17] K. Hoffmann, "An introduction to stress analysis and transducer design using strain gauges."

[18] V. Kamble, V. Shinde, and J. Kittur, "Overview of load cells," *Journal of Mechanical and Mechanics Engineering*, vol. 6, no. 3, pp. 22–29, 2020.

[19] X. Li, Z. Zhou, and J. Guo, "An unsteady aerodynamic model for three-dimensional wing based on augmented lifting-line method," vol. 127, no. 1307, pp. 97–115. [Online]. Available: https://www.cambridge.org/core/product/identifier/S0001924022000409/type/journal_article

[20] J. Silambarasan and P. Tamilamudhan, "Optimization on a 3d wing for aerodynamic lift using NACA 2412 airfoil," vol. 3, no. 1.

[21] Y. Yin, "Current study on active flow control and passive flow control," *Theoretical and Natural Science*, vol. 26, pp. 227–234, 12 2023.

[22] S. N. Joshi and Y. S. Gujarathi, "A Review on Active and Passive Flow Control Techniques," vol. 3, no. 4.

[23] G. Moscato, J. Mohamed, and G. P. Romano, "Improving performances of biomimetic wings with leading-edge tubercles," vol. 63, no. 9, p. 146. [Online]. Available: https://link.springer.com/10.1007/s00348-022-03493-8

[24] E. I. Basri, F. Mustapha, M. T. H. Sultan, A. A. Basri, M. F. Abas, M. S. A. Majid, and K. A. Ahmad, "Conceptual design and simulation validation based finite element optimisation for tubercle leading edge composite wing of an unmanned aerial vehicle," *Journal of Materials Research and Technology*, vol. 8, no. 5, pp. 4374–4386, Sep. 2019. [Online]. Available: https://linkinghub.elsevier.com/retrieve/pii/S2238785419301413

[25] I. Fernandes, Y. Sapkota, T. Mammen, A. Rasheed, C. Rebello, and Y. H. Kim, "Theoretical and Experimental Investigation of Leading Edge Tubercles on the Wing Performance," in *2013 Aviation Technology, Integration, and Operations Conference*. Los Angeles, CA: American Institute of Aeronautics and Astronautics, Aug. 2013. [Online]. Available: https://arc.aiaa.org/doi/10.2514/6.2013-4300

[26] M. A. Shorbagy, B. El-hadidi, G. El-Bayoumi, O. Said, and M. Fouda, "Experimental Study on Bio-Inspired Wings with Tubercles," in *AIAA Scitech 2019 Forum*. San Diego, California: American Institute of Aeronautics and Astronautics, Jan. 2019. [Online]. Available: https://arc.aiaa.org/doi/10.2514/6.2019-0848

[27] I. Ali, T. Hussain, I. N. Unar, L. Kumar, and I. U. Ahad, "Turbulence model study for aerodynamic analysis of the leading edge tubercle wing for low Reynolds number flows," *Heliyon*, vol. 10, no. 11, p. e32148, Jun. 2024. [Online]. Available: https://linkinghub.elsevier.com/retrieve/pii/S2405844024081799

[28] K. L. Hansen, R. M. Kelso, and B. B. Dally, "Performance variations of leading-edge tubercles for distinct airfoil profiles," *Journal of Aerospace Engineering*, 2025.

[29] A. Abdel Gawad, "Numerical simulation of the effect of leading-edge tubercles on the flow characteristics around an airfoil," 11 2012.

[30] K. Duraisamy, W. McCroskey, and J. Baeder, "Analysis of wind tunnel wall interference effects on subsonic unsteady airfoil flows," *Journal of Aircraft*, vol. 44, 09 2007.

[31] B. Kunya, C. Folayan, G. Pam, F. Anafi, and N. Muhammad, "Experimental and numerical study of the effect of varying sinusoidal bumps height at the leading edge of the nasa ls (1)-0413 airfoil at low reynolds number," *CFD Letters*, vol. 11, pp. 129–144, 01 2019.

[32] Korkmaz, Göv, and M. H. Doğru, "AERODYNAMIC ANALYSES OF NACA 63-215," *Engineering Sciences*, 2020.

[33] P. Katare and S. Sapre, "CFD analysis and wind tunnel experimental validation of NACA4412 airfoil," vol. 6, no. 3.

[34] LearnCAx, "Basics of y-plus, boundary layer, and wall function in turbulent flows," n.d., accessed: 2024-12-18. [Online]. Available: https://www.learncax.com/knowledge-base/blog/by-category/cfd/basics-of-y-plus-boundary-layer-and-wall-function-in-turbulent-flows

[35] I. Shukla, S. S. Tupkari, A. K. Raman, and A. N. Mullick, "Wall y+ approach for dealing with turbulent flow through a constant area duct," pp. 144–153. [Online]. Available: https://pubs.aip.org/aip/acp/article/1440/1/144-153/817556

[36] H. Glauert, "Wind tunnel interference on wings, bodies and airscrews."

[37] R. G. JOPPA, "Wall interference effects in wind-tunnel testing of stol aircraft," *Journal Name or Conference Name (if applicable)*, Year, accessed: 2024-12-18. [Online]. Available: https://example.com/wall-interference-stol

[38] N. Hoang and B. Bui, "Investigation of wind tunnel wall effect and wing-fuselage interference regarding the prediction of wing aerodynamics and its influence on the horizontal tail," *Journal of Mechanical Science and Technology*, vol. 33, 06 2019.

[39] A. Joulain, D. Desvigne, D. Alfano, and T. Leweke, "Numerical study of the reliability of wind-tunnel wall corrections for wingtip flow," *Journal of Aircraft*, vol. 54, pp. 1–6, 07 2016.

[40] J. T. P. Fernandes, "Design of a wind tunnel force balance."

[41] P. Lv, F. Mohd-Zawawi, E. Benard, S. Prothin, J.-M. Moschetta, and J. Morlier, "Adaptive proprotors as applied to convertible MAVs."

[42] K. C. H. V. V. S. S.-R. H.-R. Hübner, "Ucav model design and static experimental investigations to estimate control device effectiveness and s&c capabilities," *Journal Name or Platform (if applicable)*, Year, accessed: 2024-12-18. [Online]. Available: https://example.com/ucav-control-investigations

[43] B. Byam, G. Coppens, M. Dissette, K. Janson, J. Mcclain, J. Ruediger, and B. Zettel, "Formula sae design, test, tune, and setup: A design of experiment approach," *SAE Technical Papers*, 03 2003.

[44] O. S. Al-Dahiree, M. O. Tokhi, N. H. Hadi, N. R. Hmoad, R. A. R. Ghazilla, H. J. Yap, and E. A. Albaadani, "Design and shape optimization of strain gauge load cell for axial force measurement for test benches," vol. 22, no. 19, p. 7508. [Online]. Available: https://www.mdpi.com/1424-8220/22/19/7508

[45] Airfoiltools, "Airfoil database search," https://airfoiltools.com, 2024, accessed: Dec. 18, 2024.

[46] eSun, "esun pla+ filament technical data sheet," https://www.esun3d.com/uploads/eSUN_PLA%2B-Filament_TDS_V4.0.pdf, 2021, accessed: 2025-03-04.

APPENDIX

A CFD Results

A.1 Pressure Contours

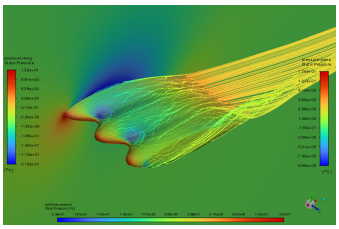

(a) 8° AOA

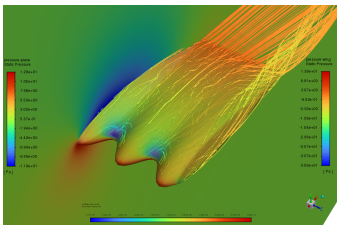

(b) 12° AOA

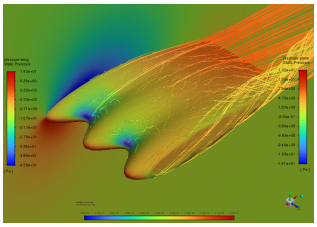

(c) 16° AOA

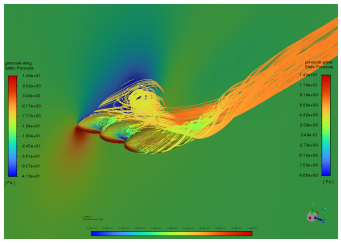

(d) 20° AOA

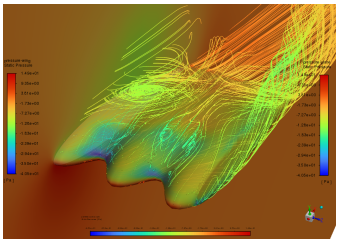

(e) 24° AOA

Figure 1: Pressure Contour of A15λ50 Wing Tubercles

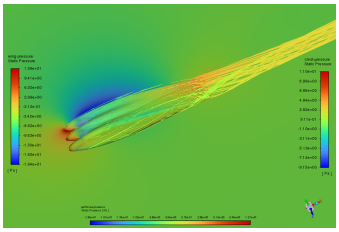

(a) 8° AOA

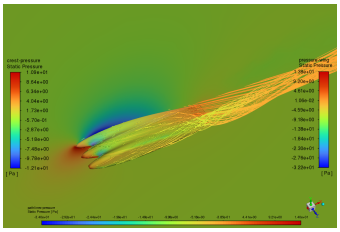

(b) 12° AOA

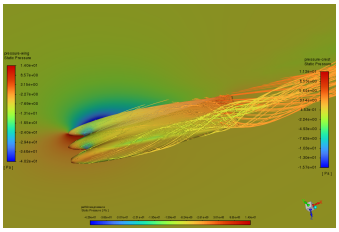

(c) 16° AOA

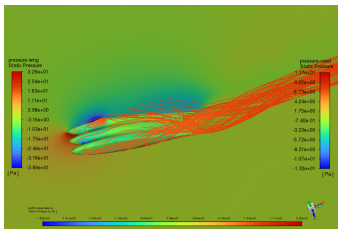

(d) 20° AOA

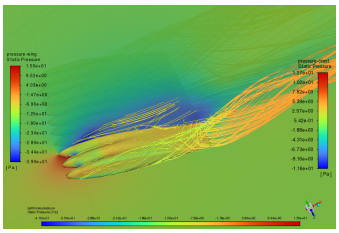

(e) 24° AOA

Figure 2: Pressure Contour of A15λ25 Wing Tubercles

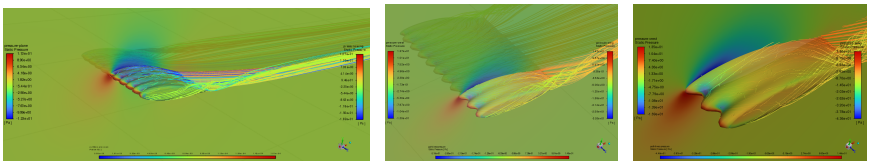

(a) 8° AOA (b) 12° AOA (c) 16° AOA

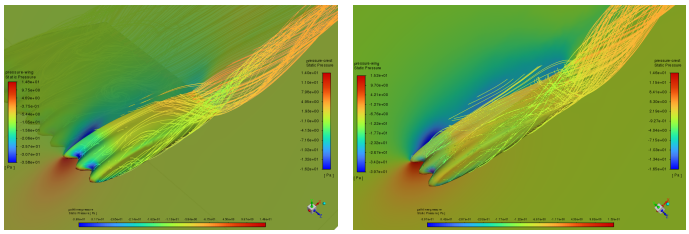

(d) 20° AOA (e) 24° AOA

Figure 3: Pressure Contour of A7.5λ25 Wing Tubercles

A.2 Velocity Contours

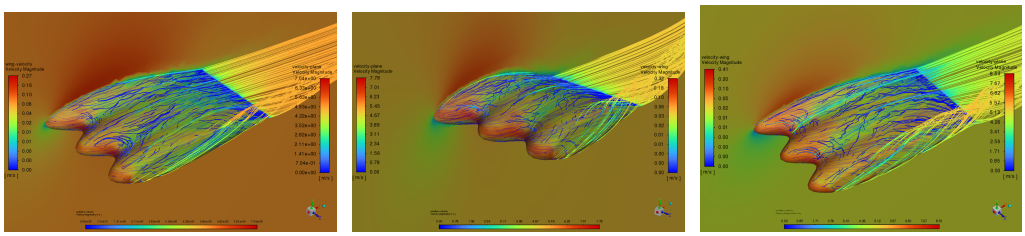

(a) 8° AOA (b) 12° AOA (c) 16° AOA

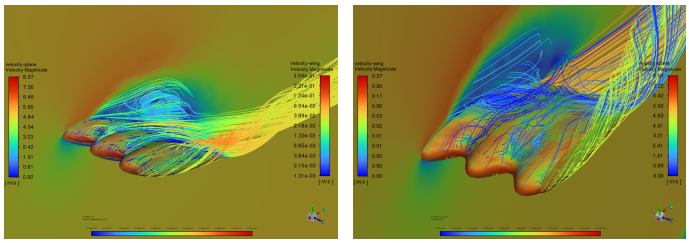

(d) 20° AOA (e) 24° AOA

Figure 4: Velocity Contour of A15λ50 Wing Tubercles

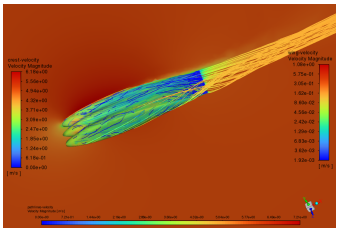

(a) 8° AOA

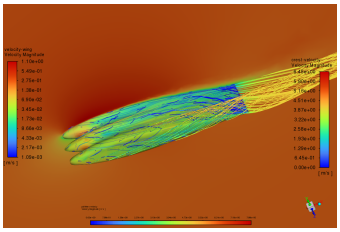

(b) 12° AOA

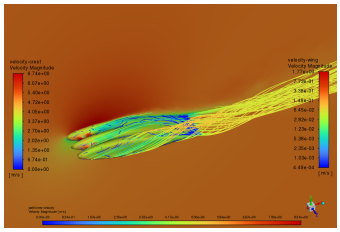

(c) 16° AOA

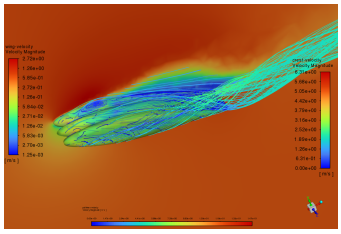

(d) 20° AOA

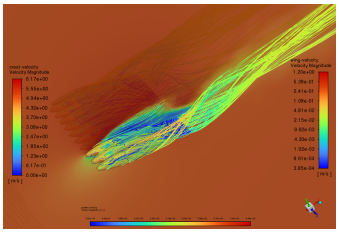

(e) 24° AOA

Figure 5: Velocity Contour of A15λ25 Wing Tubercles

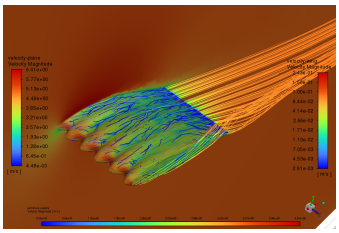

(a) 8° AOA

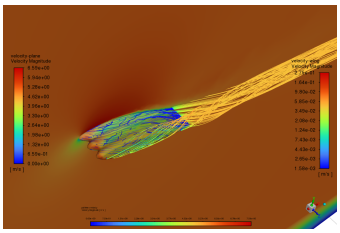

(b) 12° AOA

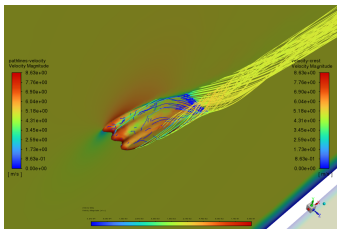

(c) 16° AOA

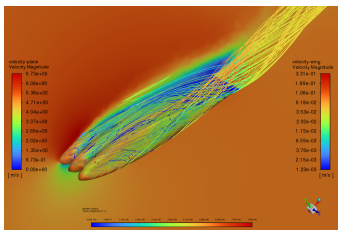

(d) 20° AOA

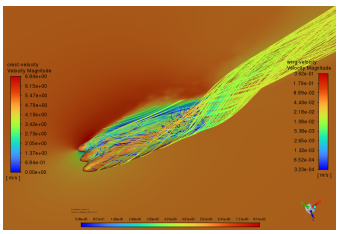

(e) 24° AOA

Figure 6: Velocity Contour of A7.5λ25 Wing Tubercles

A.3 Turbulent Kinetic Energy

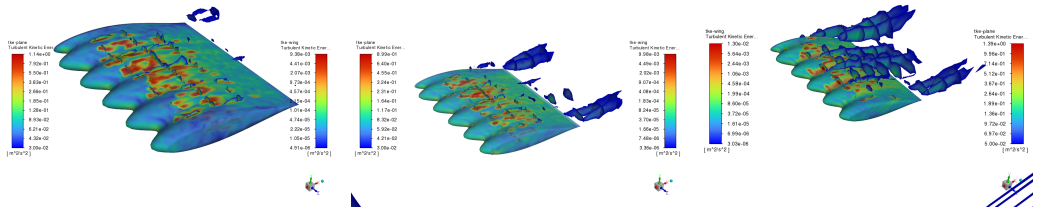

(a) 8° AOA (b) 12° AOA (c) 16° AOA

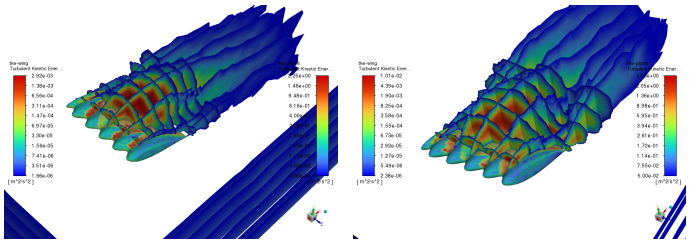

(d) 20° AOA (e) 24° AOA

Figure 7: TKE of A15λ50 Wing Tubercles

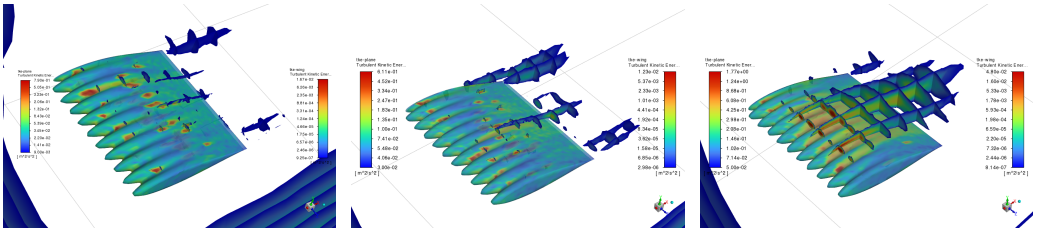

(a) 8° AOA (b) 12° AOA (c) 16° AOA

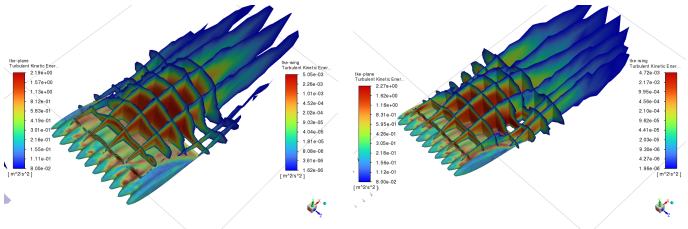

(d) 20° AOA (e) 24° AOA

Figure 8: TKE of A15λ25 Wing Tubercles

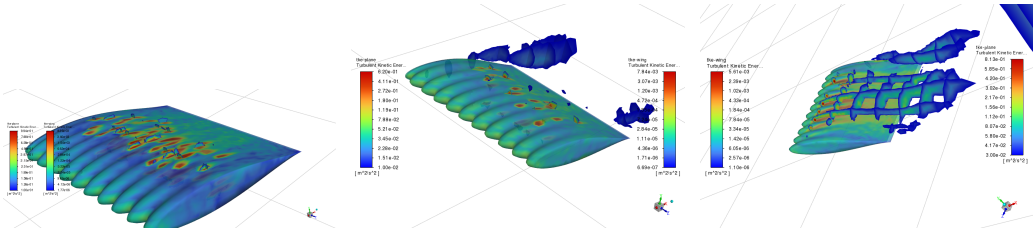

(a) 8° AOA (b) 12° AOA (c) 16° AOA

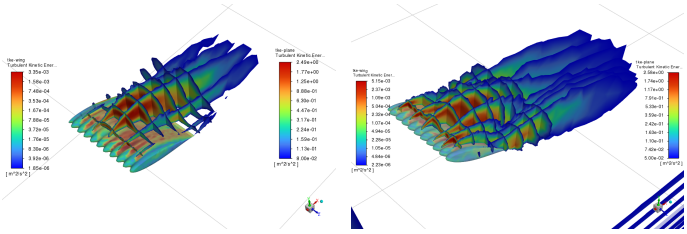

(d) 20° AOA (e) 24° AOA

Figure 9: TKE of A7.5λ25 Wing Tubercles

A.4 Vorticity Distribution

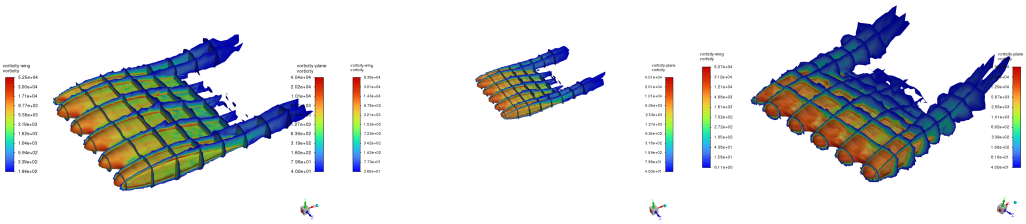

(a) 8° AOA (b) 12° AOA (c) 16° AOA

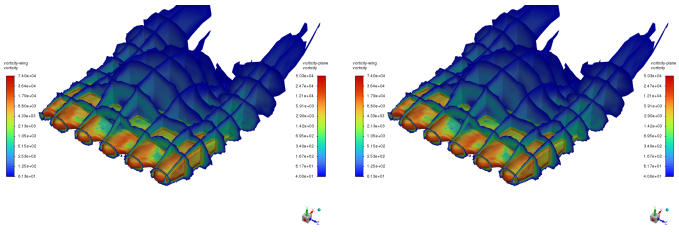

(d) 20° AOA (e) 24° AOA

Figure 10: Vorticity of A15λ50 Wing Tubercles

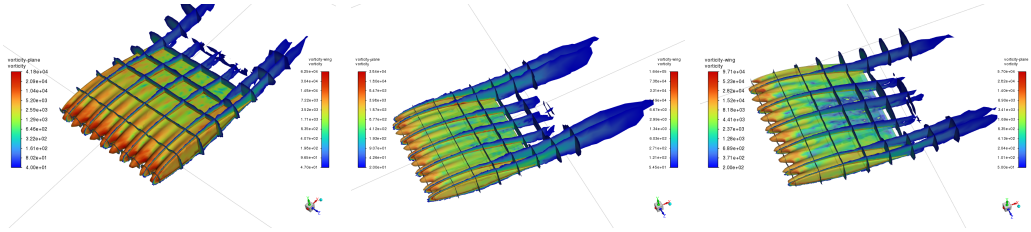

(a) 8° AOA (b) 12° AOA (c) 16° AOA

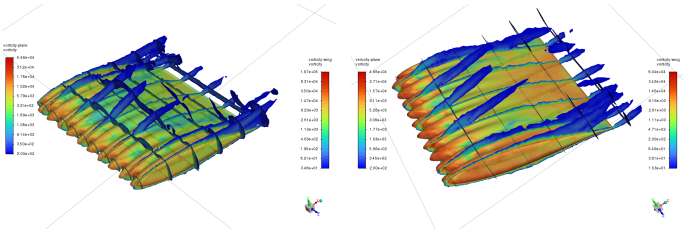

(d) 20° AOA (e) 24° AOA

Figure 11: Vorticity of A15λ25 Wing Tubercles

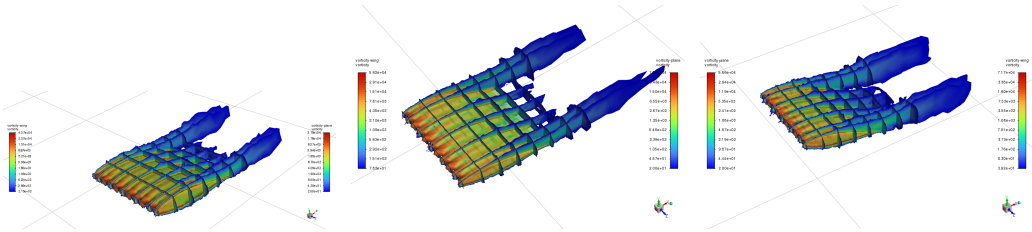

(a) 8° AOA (b) 12° AOA (c) 16° AOA

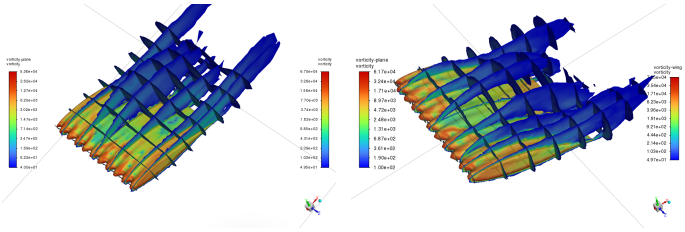

(d) 20° AOA (e) 24° AOA

Figure 12: Vorticity of A7.5λ25 Wing Tubercles